

# Azimuthal anisotropy beneath southern Africa from very broad-band surface-wave dispersion measurements

Joanne M.-C. Adam<sup>1,2</sup> and Sergei Lebedev<sup>1</sup>

<sup>1</sup>School of Cosmic Physics, Geophysics Section, Dublin Institute for Advanced Studies, 5 Merrion Square, Dublin 2, Ireland. E-mail: joanne@cp.dias.ie

<sup>2</sup>Department of Geology, Museum Building, Trinity College Dublin, Dublin 2, Ireland

Accepted 2012 June 17. Received 2012 May 29; in original form 2012 January 18

## SUMMARY

Seismic anisotropy within the lithosphere of cratons preserves an important record of their ancient assembly. In southern Africa, anisotropy across the Archean Kaapvaal Craton and Limpopo Belt has been detected previously by observations of *SKS*-wave splitting. Because *SKS*-splitting measurements lack vertical resolution, however, the depth distribution of anisotropy has remained uncertain. End-member interpretations invoked the dominance of either anisotropy in the lithosphere (due to the fabric formed by deformation in Archean or Palaeoproterozoic orogenies) or that in the asthenosphere (due to the fabric formed by the recent plate motion), each with significant geodynamic implications.

To determine the distribution of anisotropy with depth, we measured phase velocities of seismic surface waves between stations of the Southern African Seismic Experiment. We applied two complementary measurement approaches, very broad-band cross-correlation and multimode waveform inversion. Robust, Rayleigh- and Love-wave dispersion curves were derived for four different subregions of the Archean southern Africa in a period range from 5 s to 250–400 s (Rayleigh) and 5 s to 100–250 s (Love), depending on the region. Rayleigh-wave anisotropy was determined in each region at periods from 5 s to 150–200 s, sampling from the upper crust down to the asthenosphere. The jackknife method was used to estimate uncertainties, and the *F*-test to verify the statistical significance of anisotropy.

We detected strong anisotropy with a N–S fast-propagation azimuth in the upper crust of the Limpopo Belt. We attribute it to aligned cracks, formed by the regional, E–W extensional stress associated with the southward propagation of the East African Rift. Our results show that it is possible to estimate regional stress from short-period, surface wave anisotropy, measured in this study using broad-band array recordings of teleseismic surface waves.

Rayleigh-wave anisotropy at 70–120 s periods shows that the fabric within the deep mantle lithosphere of the Limpopo Belt and northern Kaapvaal Craton is aligned parallel to the Archean–Palaeoproterozoic sutures at block boundaries. This confirms that the fabric within the lithosphere created by pervasive ancient deformation is preserved to this day. Suture-parallel fabric is absent, however, in the deep lithosphere of the western Kaapvaal Craton, suggesting that it was not reworked in the collision with the craton's core, either due to its mechanical strength or because the deformation mechanism was different from those that operated in the north. Anisotropy at periods greater than 120–130 s shows fast directions parallel to the plate motion and indicates shear wave anisotropy in the asthenosphere.

The depth distribution of anisotropy revealed by surface wave measurements comprises elements of both end-member models proposed previously: anisotropy in the asthenosphere shows fast-propagation directions parallel to the plate motion; anisotropy in the Limpopo and northern Kaapvaal lithosphere shows fast directions parallel to the Archean–Palaeoproterozoic sutures. The distribution of *SKS*-splitting orientations across southern Africa reflects anisotropic fabric both within the lithosphere (dominating the splitting beneath the Limpopo Belt and northern Kaapvaal Craton) and within the asthenosphere (dominating beneath the western Kaapvaal Craton).

**Key words:** Surface waves and free oscillations; Seismic anisotropy; Cratons; Africa.

## 1 INTRODUCTION

The study of cratons (the ancient cores of continents) takes us as far back in time as the Archean Eon, over 2.5 billion years before present. The rocks within the lithosphere of cratons preserve a record of their Archean formation and evolution. The rocks' anisotropic fabric, in particular, is an indicator of the patterns of deformation during the enigmatic assembly of cratons. Such fabric gives rise to azimuthal seismic velocity anisotropy (directional dependence of seismic wave speeds) and causes detectable perturbations in the propagation of seismic waves that traverse it within the crust and underlying mantle. The character and the lateral and vertical variability of the fabric can thus be determined from seismic observations, yielding important information on how cratons evolved.

The Archean Kaapvaal Craton in southern Africa (Fig. 1) is large ( $1.2 \times 10^6$  km<sup>2</sup>) and offers abundant (and well-studied) kimberlite nodules from the deep lithosphere. It has also been sampled by a dense array of broad-band seismic stations, the Southern African Seismic Experiment (SASE), making it an exceptional natural laboratory for the study of ancient continents (De Wit *et al.* 1992; Carlson *et al.* 2000; James *et al.* 2001; Silver *et al.* 2001; Schutt & Leshner 2010). The oldest crustal ages in the western and central parts of the craton are 2.9–3.2 Ga and 3.0–3.6 Ga, respectively, and the bulk of its mantle lithosphere has probably formed prior to 3 Ga (Griffin *et al.* 2004). The older, eastern part of the Kaapvaal Craton stabilized before 2.8–3.0 Ga; its western and northern parts, as well as the Limpopo Belt adjacent to it on the north, are thought to have accreted to it in convergent-margin processes between about 2.9 and 2.6 Ga in the late Archean or, for the Limpopo Belt, around 2.0 Ga in the Palaeoproterozoic (de Wit *et al.* 1992; Kamber *et al.* 1995;

Holzer *et al.* 1998; Irvine *et al.* 2001; Moser *et al.* 2001; Schmitz *et al.* 2004; Silver *et al.* 2004).

As most Archean cratons, the Kaapvaal Craton and the Limpopo Belt are underlain by a thick, cold, stable mantle lithosphere, compositionally buoyant due to its depletion in basaltic components (Jordan 1975, 1988; Carlson *et al.* 2000; Begg *et al.* 2009; Muller *et al.* 2009; Fullea *et al.* 2011). Anomalously high *S*- and *P*-wave velocities beneath the Kaapvaal Craton and the Limpopo Belt reflect anomalously low temperatures within the mantle beneath them and show that their lithosphere currently extends down to at least 180–200 km depths (e.g. James *et al.* 2001; Fouch *et al.* 2004a; Priestley *et al.* 2006; Chevrot & Zhao 2007; Wang *et al.* 2008; Begg *et al.* 2009; Priestley & Tilmann 2009; Fishwick 2010; Adams & Nyblade 2011; Li 2011). Mantle xenolith data sample the temporal evolution of the lithosphere since its formation. They show that most of the Kaapvaal Craton and Limpopo Belt mantle root (down to 180–200 km depths) has formed and stabilized in the Archean Eon, and that it has been attached to the overlying crust since that time (Pearson *et al.* 1995; Carlson *et al.* 1999, 2000; Griffin *et al.* 2004).

According to seismic receiver function and surface wave studies, the crust beneath the northern Kaapvaal Craton and Limpopo Belt is thicker (40–45 km) than beneath the central and southwestern Kaapvaal Craton (35–40 km) (Nguuri *et al.* 2001; Stankiewicz *et al.* 2002; Nair *et al.* 2006; Yang *et al.* 2008). The world's largest layered mafic intrusion of the Bushveld Igneous Complex in the northern Kaapvaal Craton developed at around 2.06 Ga (Fig. 1) and was associated with a modification of both the crust and mantle lithosphere (Good & De Wit 1997; Carlson *et al.* 1999; Eglington & Armstrong 2004). The position of the Bushveld Complex may have been influenced by the Thabazimbi-Murchison Lineament (TML; Good & De Wit 1997), which extends across the north of the Kaapvaal craton in the NNE–SSW direction, subdividing it with faults.

A major finding of the SASE deployment of broad-band seismic stations was the peculiar distribution of *SKS* splitting across the Kaapvaal Craton and the Limpopo Belt. The splitting of *SKS* waves is an indicator of azimuthal anisotropy along their nearly vertical path from the core-mantle boundary to the seismic station. Normally, the splitting measurements are dominated by anisotropy within the lithosphere–asthenosphere system. The anisotropy reflects the crystallographic preferred orientation of olivine (the dominant mineral in the mantle) that develops in response to shear strain (e.g. Silver 1996; Savage 1999; Becker *et al.* 2006; Long & Becker 2010). In southern Africa, the splitting times (delays between the arrivals of the *SKS* waves polarized in the fast and slow propagation directions) are relatively small, around 0.6 s on average (Silver *et al.* 2001, 2004). This is about half of the global average, or of the global average over cratons only (Becker *et al.* 2012). The fast-propagation azimuths, however, displayed a coherent spatial pattern, with NE–SW fast azimuths in the western Kaapvaal Craton rotating to ENE–WSW and E–W azimuths in the northern Kaapvaal and the Limpopo Belt (Section 6). Little or no *SKS* splitting was detected in the central Kaapvaal Craton.

Silver *et al.* (2001, 2004) interpreted these fast-propagation directions as evidence that the *SKS* splitting occurs in the lithosphere. The important implication was that the splitting indicated fabric within the mantle lithosphere that formed at 2.9–2.6 Ga during collisional accretion of the western and northern parts of Kaapvaal Craton (Kimberly and Pietersburg blocks, respectively) and, later, the Limpopo Belt to the craton's core (Witwatersrand block in the central part of the craton today). This interpretation was in

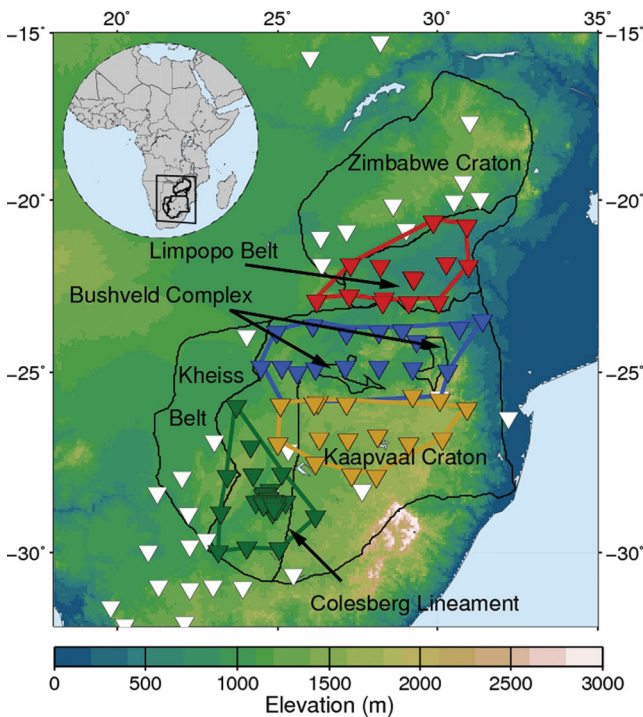


**Figure 1.** Geographic map of southern Africa, with the main tectonic units labelled. Most of the seismic stations (triangles) were deployed by SASE. The four subregions that we identify with different colours of the station symbols.

contrast to an earlier inference by Vinnik *et al.* (1995), who detected *SKS* splitting with NNE–SSW fast-propagation directions at stations within the southern Kaapvaal Craton and concluded that the splitting reflected the shear in the mantle associated with the current motion of the African Plate.

Silver *et al.* (2001, 2004) postulated that the *SKS* splitting originates in the lithosphere because a significant proportion of their measurements (particularly, the E–W ones in northern Kaapvaal and Limpopo) did not match the plate-motion direction. Their measurements in the western Kaapvaal, however, showed NE–SW and NNE–SSW fast directions, similarly to the data of Vinnik *et al.* (1995), implying an ambiguity in what the *SKS* splitting may indicate (Archean fabric in the lithosphere or recent shear beneath it?). Fundamentally, the ambiguity is due to the lack of vertical resolution inherent in *SKS* measurements. To determine the vertical distribution of anisotropic fabric beneath southern Africa, measurements of different types are required.

Surface waves can provide the necessary vertical resolution. Global and continent-scale tomographic models derived from surface wave observations have been successful in mapping the layering of azimuthal anisotropy within continental lithosphere and asthenosphere at large scales (e.g. Simons *et al.* 2002; Debayle *et al.* 2005; Yuan & Romanowicz 2010). Analysis of surface wave data from dense broad-band arrays has been producing increasingly high resolution of distributions of anisotropy, both lateral and vertical (Pedersen *et al.* 2006; Yang & Forsyth 2006; Zhang *et al.* 2007; Deschamps *et al.* 2008a; Beghein *et al.* 2010; Fry *et al.* 2010; Endrun *et al.* 2011; Lin *et al.* 2011).

In southern Africa, a number of surface wave studies targeted the isotropic shear-speed structure of the lithosphere, all detecting a thick, high-velocity root beneath the Archean cratons (e.g. Priestley 1999; Freybourger *et al.* 2001; Saltzer 2002; Li & Burke 2006; Priestley *et al.* 2006; Yang *et al.* 2008; Fishwick 2010; Adams *et al.* 2011; Fishwick & Bastow 2011; Li 2011). Radial anisotropy, determined by joint inversions of Rayleigh- and Love-wave measurements, was found to be similar in amplitude to the global average (Dziewonski & Anderson 1981), as for cratons elsewhere (Lebedev *et al.* 2009), with horizontally polarized shear waves travelling a few per cent faster than vertically polarized ones (Freybourger *et al.* 2001; Saltzer 2002). Measurements of azimuthal anisotropy, however, have proven difficult. Freybourger *et al.* (2001) searched for but did not detect azimuthal surface wave anisotropy. Li (2011) inverted Rayleigh-wave measurements for isotropic phase-velocity maps and the whole-region average phase-velocity anisotropy and found predominantly NE–SW fast-propagation directions in a 40–110 s period range, with amplitudes mostly under 1 per cent. Interestingly, Pn measurements in the central Kaapvaal Craton indicated similar, NNE–SSW fast-propagation directions within the uppermost mantle, although the small data set available was not sufficient to isolate completely the signal of anisotropy from that of isotropic heterogeneity (Kwadiba *et al.* 2003). Overall, 3-D variations of azimuthal anisotropy beneath southern Africa are still unknown.

In this study, we apply powerful recent implementations of interstation measurement methods to the complete SASE data set and measure phase velocities of the Rayleigh and Love fundamental modes in broad period ranges. Analysis of the new measurements reveals the lateral and vertical distribution of azimuthal anisotropy across the Kaapvaal Craton and the Limpopo Belt, from the upper crust down to the asthenosphere. We reconcile our results qualitatively with published shear wave splitting measurements, identify the likely depth ranges of the origin of the splitting and discuss the

implications of the results for southern Africa's lithospheric and asthenospheric dynamics.

## 2 PHASE VELOCITIES

### 2.1 Measurements

We collected seismograms recorded by two permanent (Geotech KS-54000 borehole seismometers) and 112 temporary (STS2) broad-band stations in southern Africa (Fig. 1). The temporary stations belonged to the SASE which included two deployments: the Anatomy of an Archean Craton (55 broad-band seismic stations at 82 sites) and the Kimberley Telemetered Array (30 temporary stations; Carlson *et al.* 1996). We apply a small ( $-0.688$  s) 'Quatterra bug' timing correction (Bolton *et al.* 1998) to the long-period channel data from the two permanent stations, BOSA and LBTB. All seismograms underwent instrumental response correction to displacement. The horizontal components were rotated to the radial and transverse components.

We use two methods to obtain Rayleigh- and Love-wave dispersion curves for pairs of stations in a broad range of periods. With the first method, we compute the cross-correlation of the displacement field from a source recorded at two stations (Meier *et al.* 2004) that are aligned with the source (within a backazimuth window of a  $10^\circ$  half-width). Thanks to its elaborate scheme of windowing and weighting in the time and frequency domains, this method enables measurements of interstation dispersion curves from short (5–20 s) to long (up to hundreds of seconds) periods, from the phase of the cross-correlation function. Short-period teleseismic surface waves are always diffracted and often show distinct multiple arrivals of the fundamental mode (multipathing). These waves would be difficult to model accurately with any techniques and models available. It turns out, however, that if the complex wavefield does not change too much between nearby stations, then the cross-correlation of the diffracted surface waves recorded at these stations can produce robust, accurate phase-velocity measurements (Meier *et al.* 2004; Endrun *et al.* 2008; Lebedev *et al.* 2009).

The second method uses the Automated Multimode Inversion of surface and *S* waveforms (Lebedev *et al.* 2005) that, for successful waveform fits, can measure average phase velocities between sources and stations. Dispersion curves that average between pairs of stations are then computed from these 'source-station' dispersion curves, with the stations and sources, again, approximately on the same great-circle path (Lebedev *et al.* 2006). This method is complementary to the first one in that it provides more phase-velocity measurements at long periods (over 50 s), at which the fundamental mode often interferes with *S* and multiple-*S* arrivals, especially for Love waves, making cross-correlation measurements difficult. Dispersion curves from both methods and all earthquakes are then combined, and an average curve can be computed for each station pair.

We use transverse and vertical components to measure phase-velocity curves for Love and Rayleigh waves, respectively. Measurements are carefully examined interactively, to remove any rough (not smooth) portions of dispersion curves and outliers. Surface-wave diffraction and mode interference may cause errors in phase-velocity measurements performed on seismograms from any single event (e.g. Friederich *et al.* 2000; Pedersen 2006; Bodin & Maupin 2008). Because these effects have a strong frequency dependence, selection of only smooth portions of phase-velocity curves reduces the impact of the errors. The averaging of many measurements,

performed on signal from events in different regions, particularly at opposite azimuths from the station–station pair, is another important element of the method and produces robust, accurate phase-velocity measurements (Meier *et al.* 2004; Lebedev *et al.* 2006).

## 2.2 The four subregions

A robust phase-velocity curve for a pair of stations can be computed as an average over tens to hundreds of curves measured using seismograms from single events (Meier *et al.* 2004; Lebedev *et al.* 2006). If average dispersion curves are computed for various station combinations within an array, a tomographic inverse problem can be set up and solved for the distributions of the isotropic and anisotropic heterogeneity (e.g. Zhang *et al.* 2007; Deschamps *et al.* 2008a; Endrun *et al.* 2011). Because of the relatively short deployment time of the SASE stations and the remoteness of southern Africa from regions of abundant seismicity, there are not enough ‘one-event’ measurements to compute robust averages for most of the pairs of SASE stations.

We thus devise an alternative approach: we divide southern Africa into subregions, each with a relatively homogeneous structure within it, and invert our measurements for subregion-average, phase-velocity structure and anisotropy. The four regions we identify are the Limpopo Belt and the northern, central and southwestern Kaapvaal Craton (Fig. 1). The crustal thickness is relatively uniform within each of the subregions, according to published receiver-function and surface wave studies (Nguuri *et al.* 2001; Stankiewicz *et al.* 2002; Nair *et al.* 2006; Yang *et al.* 2008; Kgaswane *et al.* 2009). Isotropic phase-velocity heterogeneity at periods sampling the crust and the mantle is also relatively weak within each subregion (Yang *et al.* 2008; Li 2011). Each of the four regions contains numerous two-station pairs (Table 1; Fig. 2, top panels) and is sampled by a very large number of phase-velocity measurements (Fig. 2, middle and bottom panels).

## 2.3 Isotropic-average, Rayleigh and Love phase-velocity curves

Using the numerous phase-velocity measurements within each of the four regions (Table 1; Fig. 2), we obtain accurate isotropic-average dispersion curves in very broad ranges of periods. The period ranges extend from 5 s to 250–400 s for Rayleigh and from 5 s to 100–250 s for Love waves, depending on the region (Figs 2 and 3). Phase-velocity measurements in such period ranges can resolve shear velocity structure from the upper crust down to the lower lithosphere and asthenosphere (Fig. 4).

In Fig. 3 we compare the phase-velocity curves from the four regions with each other, with global-reference curves, and with published previous measurements. Both Rayleigh and Love curves from the four regions are well above global average values and are, overall, very similar across the four regions (Fig. 3A). Zooming in on the differences between the regions, we plot Rayleigh-wave phase-velocity anomalies (Fig. 3B), computed as differences of observed curves and the curve computed for the reference model AK135 (Kennett *et al.* 1995), which is close to a global continental average.

Phase-velocity curves in Figs 3(A) and (B) are computed by simple averaging over all measurements within the regions. Our measurements, however, are distributed unevenly as a function of azimuth of the interstation path (specifically, paths with ~NE back-azimuths align with more events, mainly in SE Asia, than those

at other backazimuths). In the presence of azimuthal anisotropy, this may result in a bias in the average phase-velocity curves. The bias can be removed by computing both the isotropic values and anisotropy of phase velocities explicitly, as we describe in Section 3. In Figs 3(C) and (E) we plot our isotropic-average phase-velocity curves with the effect of anisotropy removed; Figs 3(D) and (F) show the anomaly of the isotropic-average curves relative to AK135. We do not plot the isotropic curves up to the very long periods spanned by the simple-average curves because the number of measurements at these periods was insufficient to compute anisotropy accurately. The effect of azimuthal anisotropy, however, is small compared to the phase-velocity anomalies relative to the global average. Therefore, for most purposes, simple-average curves (Figs 3A and B) provide useful accuracy up to the very long periods (>200 s).

In all Archean parts of southern Africa sampled by our data, phase velocities are much greater than the global average, both at the short periods that sample the crust and at the long periods that sample primarily the mantle lithosphere, indicating high shear velocities in both layers. The reduction in the anomaly at 15–30 s (Figs 3B, D and F) is in part due to the crust being thicker than the 35 km crust in the reference model (Nguuri *et al.* 2001; Stankiewicz *et al.* 2002; Nair *et al.* 2006; Yang *et al.* 2008; Kgaswane *et al.* 2009): the northern Kaapvaal Craton and the Limpopo Belt have the thickest crust and show the lowest phase velocities in this period range.

Rayleigh-wave curves published recently by other authors are consistent with our measurements. We compare the published curves and our isotropic-average ones in Figs 3(E) and (F). The smooth, southern Africa average dispersion curve of Yang *et al.* (2008) is somewhat slower than all of our curves because it was an average over a larger region around the Kaapvaal Craton, including non-cratonic, southern South Africa. The North Kaapvaal average curve of Li & Burke (2006) is nearly identical to our northern Kaapvaal and Limpopo curves in most of its 20–180 s period range (apart from its rougher portion with a dip at 70–110 s). The South Kaapvaal average curve of Li & Burke (2006) is also very similar to our central and southwestern Kaapvaal curves at 25–50 s, although it is 1–2 per cent slower at longer periods. This is probably due to their South Kaapvaal region extending further south than our subregions and sampling the seismically slower southernmost portion of the craton (Yang *et al.* 2008; Li 2011).

The Rayleigh-wave curves obtained by different methods are very similar, and the (small) differences between them can be explained by the differences in the boundaries of the regions that the curves average over. This consistency validates the measurements and confirms the accuracy of the currently available Rayleigh-wave data.

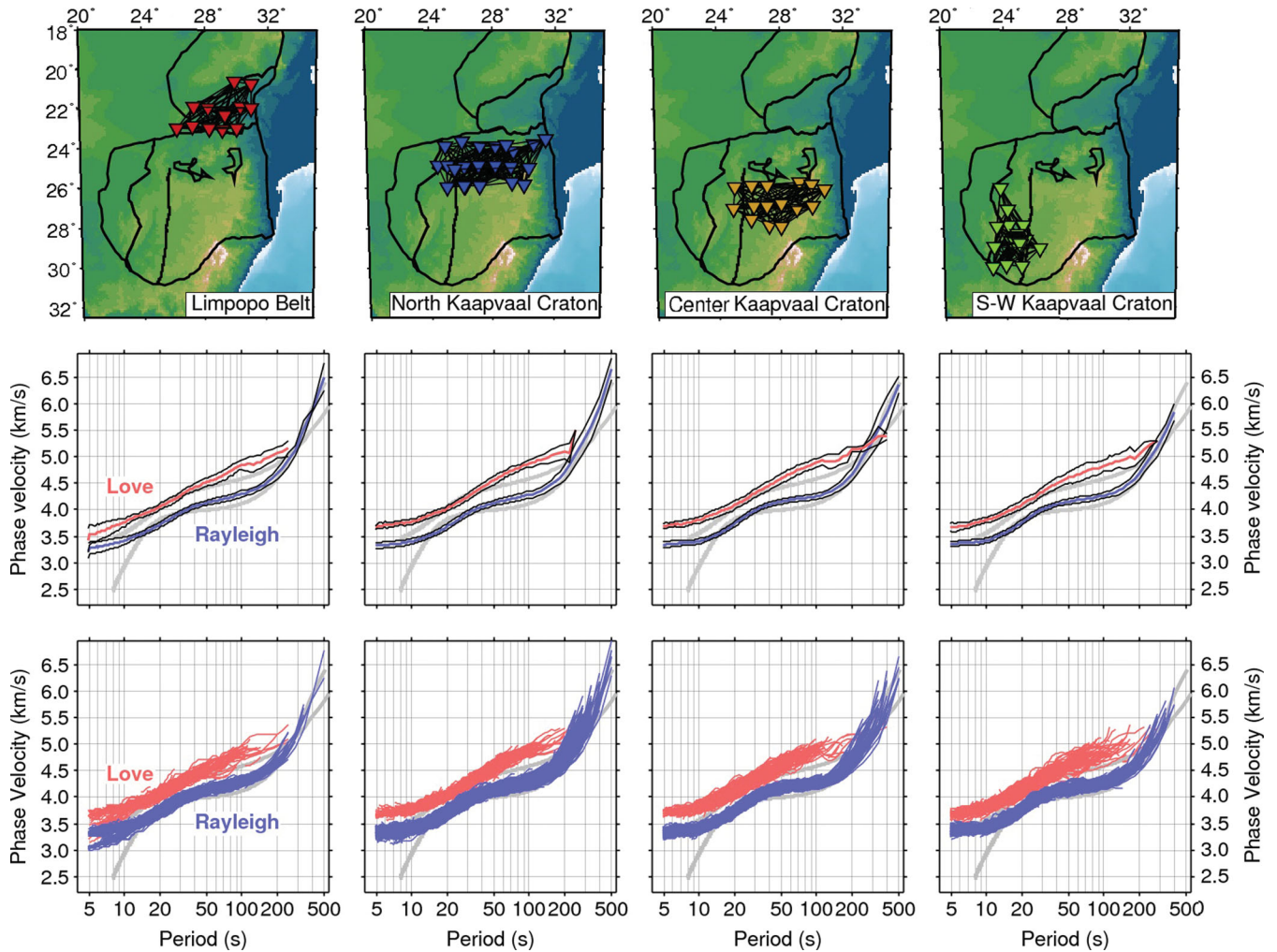
The new measurements obtained in this study extend the range of Rayleigh-wave curves to very long periods and also add the broadband Love-wave curves (Fig. 3A). The availability of both Rayleigh and Love measurements will be particularly useful for isolating the isotropic-average seismic-velocity structure from the effects of radial anisotropy, to relate it to the lithospheric temperature and composition (e.g. Khan *et al.* 2011; Fullea *et al.* 2012).

## 3 INVERSION

Within each subregion, we measured phase velocities of surface waves travelling at different azimuths. We can use the azimuthal dependence of phase velocities to determine the orientation and amplitude of azimuthal anisotropy, as a function of period, in different parts of the Kaapvaal Craton and in the Limpopo Belt.

**Table 1.** Number of stations, station pairs and Rayleigh- and Love-dispersion curves for the four subregions and the entire region.

	Number of stations	Number of station pairs	Number of Rayleigh dispersion curves	Number of Love dispersion curves
Limpopo Belt	16	112	1065	455
Northern Kaapvaal Craton	25	191	2241	500
Central Kaapvaal Craton	18	113	1119	431
Southwestern Kaapvaal Craton	34	190	1222	530
Southern Africa	88	618	6188	2083

**Figure 2.** Rayleigh- and Love-phase velocity measurements. Top panels: stations and interstation paths within each subregion. Middle panels: region-average, phase-velocity curves for Love and Rayleigh waves. Bottom panels: all dispersion curves, each measured using a pair of stations and a single event. Grey dispersion curves were computed for the reference model AK135 (Kennett *et al.* 1995).

### 3.1 Rayleigh-wave anisotropy

The azimuthal data coverage is sufficient to constrain azimuthal anisotropy in the period range from 5 s to 150–200 s, depending on the region. The inversion procedure described later is applied independently to data from each subregion, at every period.

First, we sort phase-velocity measurements into  $1^\circ$  bins, according to the station–station azimuth. For example, the north–south direction ( $0^\circ$ ) contains interstation pairs with azimuths in the range  $[-0.5^\circ; 0.5^\circ]$ . We next use sliding windows to smooth the phase-

velocity distributions with azimuth. This averages out noise in the measurements and also takes into account the finite station–event backazimuth window used in the selection of sources for phase-velocity measurements. We choose the half-width of the window of  $15^\circ$ . For example, phase velocity in the north–south direction ( $0^\circ$ ), is an average over all measurements from all interstation pairs situated at azimuths in the range  $[-15.0^\circ; 15.0^\circ]$ . Such a  $30^\circ$  width window is applied at every  $1^\circ$  step. We have verified that the choice of the width of the window does not influence our results (in Appendix A, we test three different window widths and show that the results

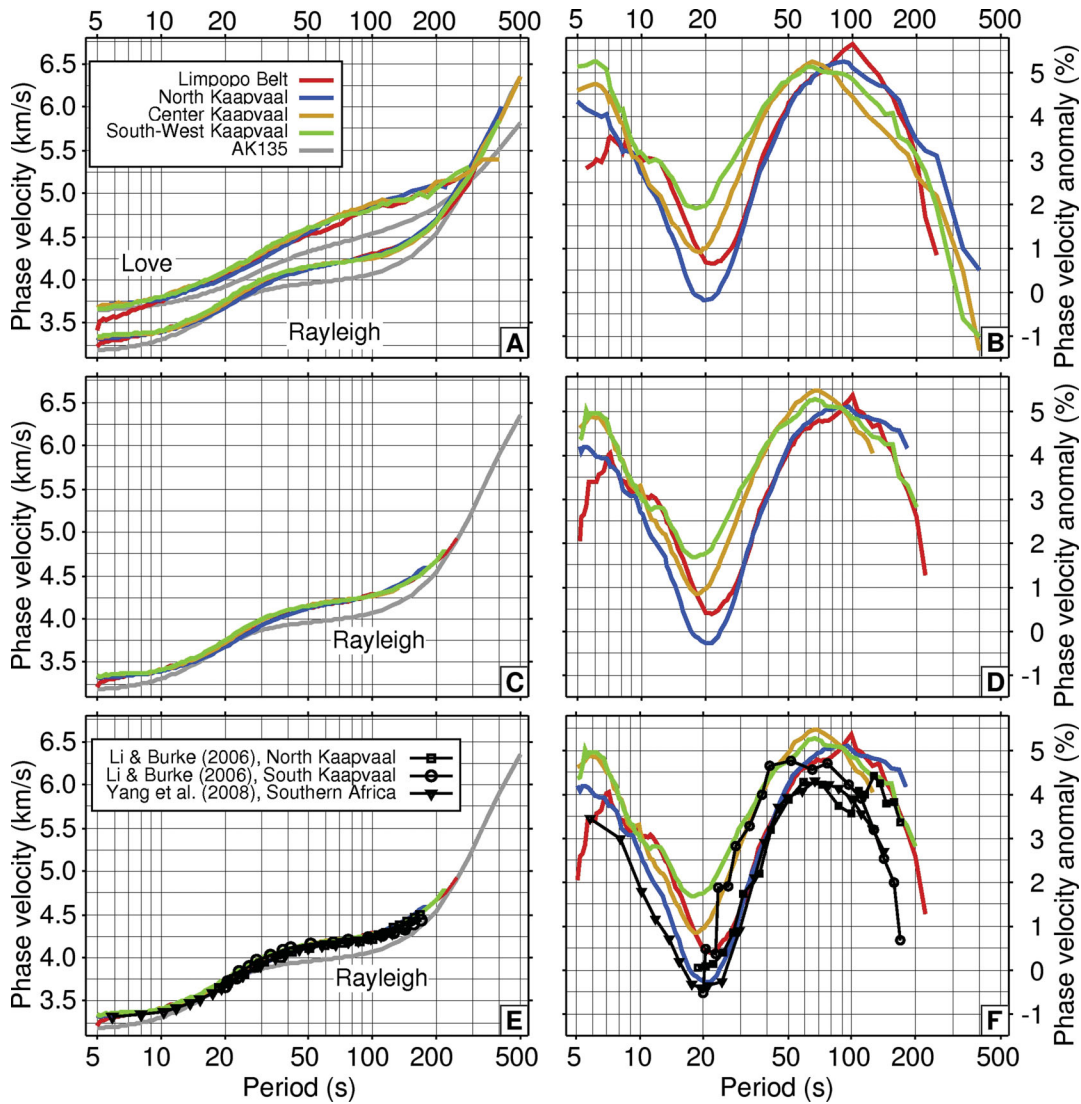


**Figure 3.** Subregion-average dispersion curves. (A) Rayleigh- and Love-wave dispersion curves for the four subregions, computed by simple averaging. (B) Same Rayleigh-wave dispersion curves as in panel (A) but presented as the anomaly with respect to AK135 (Kennett *et al.* 1995), to highlight the differences between the curves. (C) Isotropic-average, Rayleigh-wave dispersion curves for the four subregions, computed by inversions for azimuthal anisotropy at each period. (D) Same curves as in panel (C) but presented as the anomaly with respect to AK135. (E) Comparison between our isotropic curves (same as in C) and those from previous studies. (F) Same curves as in panel (E) but presented as the anomaly with respect to AK135.

are robust with respect to the choice of the width). To avoid biases due to larger numbers of measurements at some azimuths compared to others, phase velocity in a window is computed as a weighted average, with weights inversely proportional to the number of measurements at an azimuth. At a period  $T$  and azimuth  $\varphi$ , the averaged phase velocity  $C(T, \varphi)$  is computed as:

$$C(T, \varphi) = \frac{1}{\sum_i w_i(T)} \sum_{i=\varphi-15}^{\varphi+15} w_i(T) \cdot \sum_j C_j(T, i), \quad (1)$$

with

$$w_i(T) = \frac{1}{n_i(T)}, \quad (2)$$

where  $w_i(T)$  is the weight applied at the azimuth  $i$  ( $i \in \mathbb{Z}$ ) and  $n_i(T)$  is the number of measurements at azimuth  $i$ .  $C_j(T, i)$  is the  $j$ th phase-velocity measurement at the azimuth  $i$  and period  $T$ .

For a weakly anisotropic medium, azimuthal anisotropy of surface waves is described (Smith & Dahlen 1973) as a harmonic function of the form:

$$C(T, \varphi) = C_0(T) + A_1(T) \cos(2\varphi) + A_2(T) \sin(2\varphi) + A_3(T) \cos(4\varphi) + A_4(T) \sin(4\varphi), \quad (3)$$

where  $T$  is the period,  $\varphi$  is the azimuth,  $C$  is the observed phase velocity,  $C_0$  is the isotropic phase velocity and  $A_1$ ,  $A_2$ ,  $A_3$  and  $A_4$  are variables that depend on elastic properties of the medium and parametrize anisotropy. At each period, the amplitudes of anisotropy ( $A_{2\varphi}$  and  $A_{4\varphi}$ ) and the fast-propagation azimuths ( $\phi_{2\varphi}$  and  $\phi_{4\varphi}$ ) for the  $2\varphi$  and  $4\varphi$  components of anisotropy, respectively, are calculated as:

$$A_{2\varphi} = \sqrt{A_1^2 + A_2^2}; \quad A_{4\varphi} = \sqrt{A_3^2 + A_4^2}, \quad (4)$$

$$\phi_{2\varphi} = \frac{1}{2} \text{Atan} \left( \frac{A_2}{A_1} \right); \quad \phi_{4\varphi} = \frac{1}{4} \text{Atan} \left( \frac{A_4}{A_3} \right). \quad (5)$$

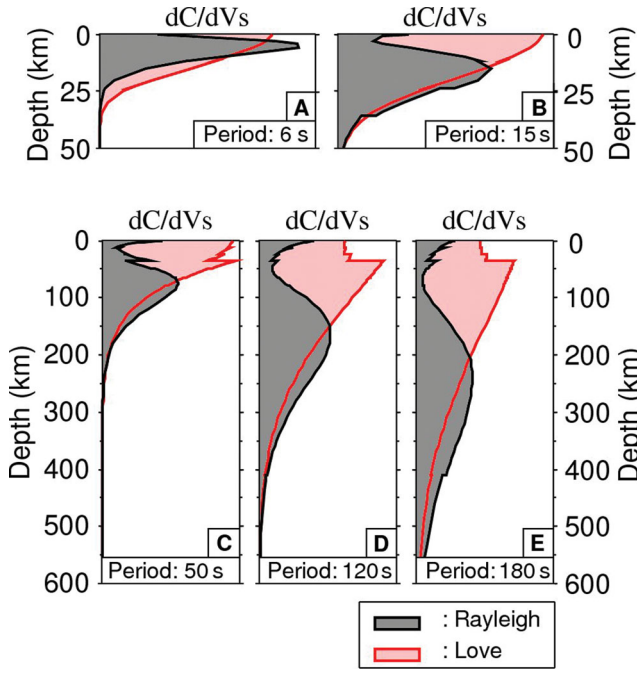


**Figure 4.** Sensitivity kernels for the fundamental mode Rayleigh- (grey) and Love- (red) wave phase velocity as a function of depth at five periods (6, 15, 50, 120 and 180 s). Each graph is scaled independently. The derivatives are computed for a model with a 37-km-thick crust.

For each period, we solve (3) as  $\mathbf{d} = \mathbf{G} \cdot \mathbf{m}$ , where  $\mathbf{d}$  is the vector that contains the data (phase velocity at each azimuth),  $\mathbf{m}$  is the vector that contains the model  $[C_0, A_1, A_2, A_3, A_4]^T$  and  $\mathbf{G}$  is the sensitivity matrix with the coefficients that link the data and the model. We use the least-squares method with damping to solve this problem. Because our problem is overdetermined, we use

$$\mathbf{m} = (\mathbf{G}^T \mathbf{C}_d^{-1} \mathbf{G})^{-1} \mathbf{G}^T \mathbf{C}_d^{-1} \mathbf{d}, \quad (6)$$

where  $\mathbf{C}_d$  is a diagonal matrix containing the *a priori* errors of the measurements. The *a priori* errors have been estimated as the standard deviation of the measurements, depending on the number of measurements per azimuth. The error  $\text{err}(T, \varphi)$  at period  $T$  and azimuth  $\varphi$  is

$$\text{err}(T, \varphi) = \sqrt{\frac{\sum_{i=1}^n (C_i(T, [\varphi - 15; \varphi + 15]) - C(T, \varphi))^2}{n}}, \quad (7)$$

where the summation is over the azimuths within the range defined by the sliding window centred on  $\varphi$ :  $[\varphi - 15; \varphi + 15]$ .  $n$  is the total number of measurements in the window. We also set a minimum error value, equal to the error at the azimuth with the most measurements.

The amplitude of anisotropy we compute is underestimated somewhat because of the sliding-window averaging (1, 2). With a dense azimuthal coverage, the underestimation is well below 10 per cent of the amplitude (as given by the application of a sliding window at an extremum of the cosine function), but the effect can be stronger if the data samples the azimuth range sparsely and unevenly. To estimate how much the amplitudes of anisotropy may be reduced, we apply our algorithm to synthetic data with a known fast direction and amplitude of anisotropy but with azimuthal coverage as in our measured data set. The largest underestimation amounts to 37 per cent of the amplitude and occurs at very long periods where the azimuthal coverage deteriorates. In the following, we plot and discuss

only robust anisotropy results, constrained by data with sufficient azimuthal coverage.

### 3.2 Love-wave anisotropy

Using the same approach as for Rayleigh waves, we also inverted our Love-wave measurements (Fig. 2) for azimuthal anisotropy. Love-wave phase velocities depend on the horizontally polarized shear velocities, and Love-wave anisotropy should be described by  $4\varphi$  terms only (Trampert & Woodhouse 2003). Surprisingly, our results showed  $2\varphi$  terms that were larger than  $4\varphi$  terms and gave fast-propagation directions similar to those of Rayleigh waves. This may have been because Love-wave measurements were influenced by the presence of Rayleigh-wave energy on transverse components.

The  $90^\circ$  periodic azimuthal variations described by the  $4\varphi$  terms (3) are generally more difficult to resolve than the  $180^\circ$  periodic ( $2\varphi$ ) ones, and any biases due to mode interference, wave front bending or uncertainties in horizontal component orientations will make the task more difficult yet. Even with the large amounts of Love-wave measurements in each region (Fig. 2), our data set does not appear to constrain Love-wave azimuthal anisotropy accurately. We thus focus on Rayleigh-wave anisotropy only.

## 4 RESOLUTION AND ERRORS

### 4.1 Jackknife

We estimate the *a posteriori* errors on the parameters of the model ( $[C_0, A_1, A_2, A_3, A_4]^T$ ) using the jackknife method (Efron & Tibshirani 1986). With this method, we obtain a first estimate of the lower bound of the error that we can expect on the parameters. The jackknife method provides error estimates by means of repeating the inversion a large number of times (one hundred times in this study), with a data set from which a randomly selected part of data (30 per cent of the phase-velocity measurements, in this study) has been removed. We remove the random set of data before averaging the data with sliding windows. The distribution of each parameter is expected to follow a Gaussian law, yielding an estimate of the mean and the interval of confidence (half-width of the Gaussian). We use this method to estimate the error on the isotropic-velocity deviation from the reference value and on the fast-propagation azimuths and amplitudes of the  $2\varphi$  and  $4\varphi$  anisotropy (5). Examples of the results in Fig. 5 show that, as expected, the values are distributed following Gaussians.

The resulting estimated errors are small for the  $2\varphi$  fast-propagation azimuth (below  $5^\circ$ ) and are larger for the  $4\varphi$  fast azimuth and the amplitudes of anisotropy. The errors increase at long periods because of the decrease in the amount of data.

### 4.2 *F*-test

#### 4.2.1 Method

To test whether anisotropy is statistically significant (whether  $2\varphi$  or  $4\varphi$  terms are required to explain the data), we perform *F*-tests.

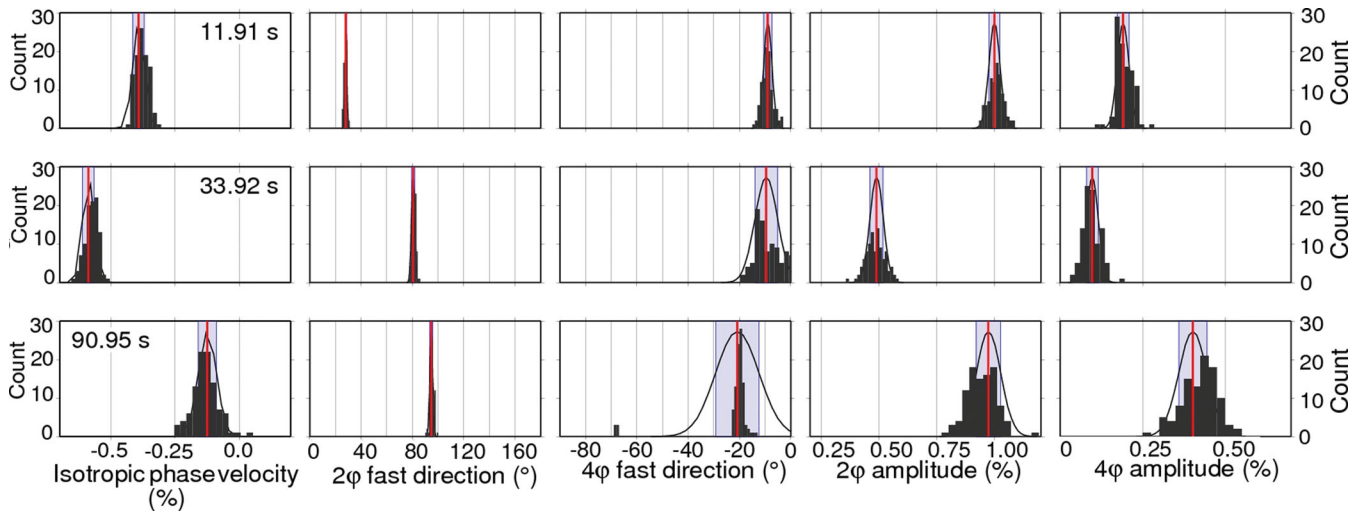


**Figure 5.** Examples of jackknife distributions of the isotropic and four anisotropic parameters in the Limpopo Belt region at three different periods. Red lines indicate the maximum of the best-fitting Gaussian. Blue areas indicate the half-width of the Gaussian, used to estimate the errors on the parameters.

To do so, we first compute the reduced  $\chi^2$  given by the azimuthal anisotropy inversion at every period:

$$\chi^2 = \frac{1}{N - \text{tr}(\mathbf{R})} (\mathbf{d} - \mathbf{G}\hat{\mathbf{m}})^T \mathbf{C}_d^{-1} (\mathbf{d} - \mathbf{G}\hat{\mathbf{m}}), \quad (8)$$

where  $N$  is the number of data and  $R$  is the resolution matrix. The resolution matrix is an identity matrix and its size is equal to the number of unknown (its size is equal to one if we consider only an isotropic inversion, three if we consider an isotropic and the  $2\varphi$  terms and five if we consider a full harmonic function like in the eq. 3). The values of  $\chi^2$  are a measure of how well the model fits the data; if the model fits the data well,  $\chi^2$  values tend to be close to 1. A comparison of  $\chi^2$  given by isotropic and anisotropic inversions (with  $2\varphi$  only or both  $2\varphi$  and  $4\varphi$  terms) should show if the data are explained significantly better with anisotropic models, compared to an isotropic one.

We use  $\chi^2$  tests instead of a comparison of variance reductions because we are comparing inversions with different degrees of freedom (an isotropic one has only one parameter and one degree of freedom; anisotropic inversions involve three or five parameters, depending on whether  $2\varphi$  only or both  $2\varphi$  and  $4\varphi$  terms are included).

We perform four series of inversions: first, for isotropic phase-velocity perturbations only; second, for isotropic and  $2\varphi$  anisotropic terms; third, for isotropic and  $4\varphi$  anisotropic terms; and fourth, for isotropic,  $2\varphi$  and  $4\varphi$  terms.  $F$ -tests are then performed to determine whether the reduction of the  $\chi^2$  between inversions with different degrees of freedom is significant or not (Bevington 1969).

The ratio of the statistics ( $\chi^2$ ) should follow the Fisher–Snedecor law distribution depending on the number of degrees of freedom in the inversions. For example, if we test whether or not a  $2\varphi$  anisotropic inversion fits the data better than an isotropic inversion, the  $F$ -test value will be:

$$F_{1,3} = \frac{\chi^2_{\text{iso}}}{1} / \frac{\chi^2_{2\varphi}}{3}, \quad (9)$$

and for a test on whether anisotropic model with both  $2\varphi$  and  $4\varphi$  terms fits better than an isotropic model it will be:

$$F_{1,5} = \frac{\chi^2_{\text{iso}}}{1} / \frac{\chi^2_{2\varphi+4\varphi}}{5}. \quad (10)$$

The greater the  $F$ -value, the more significant the  $\chi^2$  reduction. To gauge statistical significance, we compare the  $F$ -values to threshold values, which depend on the degrees of freedom and on the confidence index we choose. We set the confidence index to the commonly used value of 0.05, meaning that the  $F$ -value is 5 per cent probable to be an outlier. For a more conservative test, we also set the confidence index to 0.01 (Fig. 6); the  $F$ -value is then only 1 per cent probable to be an outlier (Bevington 1969). For the test to be significant,  $F_{1,3}$  should be at least 10.13 if a confidence index of 0.05 is assumed and at least 34.12 for a confidence index of 0.01.  $F_{1,5}$  must be at least 6.61 with a confidence index of 0.05 and at least 16.26 with a confidence index of 0.01 (Bevington 1969).

#### 4.2.2 $F$ -test results for Rayleigh waves

Fig. 6 illustrates the anisotropy patterns (A and B) constrained by the inversions of the data from the four regions for the isotropic,  $2\varphi$  and  $4\varphi$  coefficients (3) at different periods, as well as the statistical significance of anisotropy (C–E). The amplitude of anisotropy (Fig. 6, frames A and B) is given both by the position of the small circles along the  $y$ -axis and by the length of the sticks centred on the circles. The fast-propagation direction is given by the orientation of the sticks (as if on a map): vertical means N–S and horizontal means E–W. For the  $4\varphi$  patterns, only one of the two perpendicular fast directions is plotted, for clarity. In Fig. 6(C) we compare the misfits given by different inversions, parametrized using a full set as well as different subsets of the isotropic,  $2\varphi$  and  $4\varphi$  coefficients.

The  $4\varphi$  terms are very small almost everywhere, and so are the reductions in misfits that result from adding the  $4\varphi$  terms as inversion parameters (Fig. 6C). The  $4\varphi$  anisotropy is expected to be weak for long-period Rayleigh waves that sample the olivine-dominated upper mantle (Montagner & Tanimoto 1991; Trampert & Woodhouse 2003). An absence of statistically significant  $4\varphi$  anisotropy has been seen in a number of previous regional-array studies (e.g. Deschamps *et al.* 2008a; Darbyshire & Lebedev 2009), and our analysis confirms these findings.

In the crust, the  $4\varphi$  terms may play a greater role (Polat *et al.* 2012). According to our results, however, even in the Limpopo Belt, where the  $4\varphi$  terms are the largest, both their amplitude and

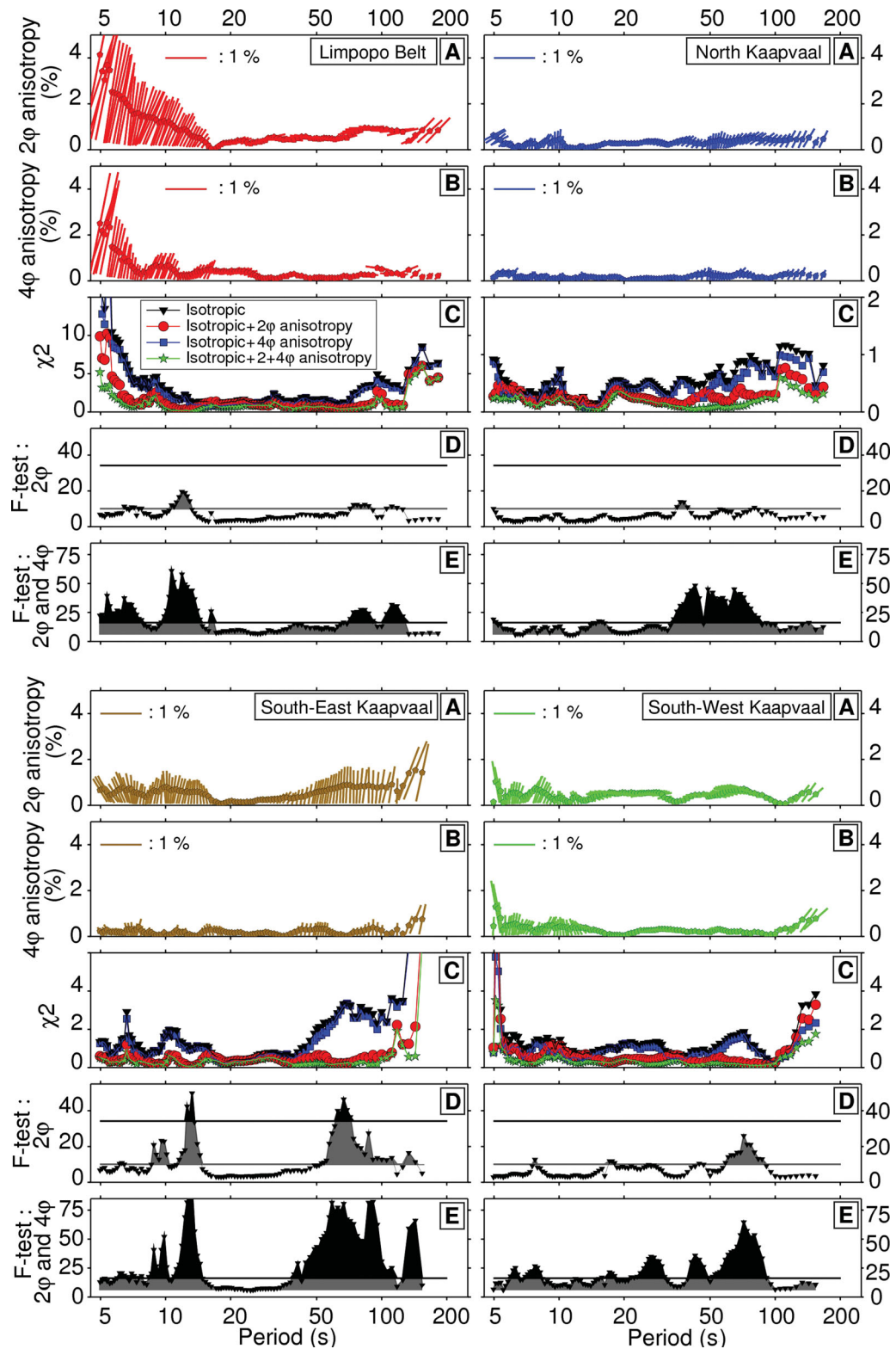


**Figure 6.** Results of the inversions and  $F$ -tests for the four subregions. (A) Azimuths of fast-propagation directions and amplitudes of anisotropy, the  $2\varphi$  terms. The inversion were for the isotropic and both the  $2\varphi$  and  $4\varphi$  terms. (B) Azimuths of fast direction and amplitudes of anisotropy, the  $4\varphi$  terms (for clarity, only one of the two perpendicular fast directions is shown). (C) Reduced  $\chi^2$  of the inversions considering only the isotropic part (black lines and triangles), the isotropic part and  $2\varphi$  anisotropy (red lines and circles), the isotropic part and  $4\varphi$  anisotropy (blue lines and squares) and the isotropic part with both  $2\varphi$  and  $4\varphi$  anisotropy (green lines and stars). (D)  $F$ -tests on whether the  $2\varphi$  terms are required, compared to an isotropic inversion. (E)  $F$ -tests on whether the  $2\varphi$  and  $4\varphi$  terms are required, compared to an isotropic inversion. Shaded areas indicate significance, according to the  $F$ -test. Grey: above a confidence index of 0.05, black: above a confidence index of 0.01.

statistical significance are well below those of the dominant  $2\varphi$  terms. In the following, we shall thus discuss and interpret only the  $2\varphi$  anisotropy patterns.

Inversions with both  $2\varphi$  and  $4\varphi$  terms included can produce  $F$ -values that are much larger compared to those from inversions without anisotropy (Figs 6 and B1). These  $F$ -values are also substantially larger than the  $F$ -values from inversions with either  $2\varphi$  or  $4\varphi$  terms only. The addition of the  $4\varphi$  terms by itself, however, produces only a small reduction in the misfits, as illustrated by Fig. 6(C) and also by our additional  $F$ -tests, presented in Appendix B for completeness. The only exception is in the period range 33–83 s for the North Kaapvaal Craton region, where adding  $4\varphi$  anisotropy to the  $2\varphi$  anisotropy improves the fit significantly (Fig. B1, frames C).

The  $\chi^2$  misfits (Fig. 6, frames C) show that the introduction of anisotropy reduces misfits substantially in some period ranges. At other periods, an isotropic model is sufficient to explain the data, with the  $\chi^2$  values given by isotropic inversions close to 1.

$F$ -test results (Figs 6D and E) indicate whether or not adding  $2\varphi$  (D) or  $2\varphi$  and  $4\varphi$  (E) anisotropy to the models improves the fit to the data, compared to an isotropic model. The northern Kaapvaal Craton does not show significant anisotropy at short periods. Phase-velocity anisotropy in the Limpopo Belt and southern Kaapvaal regions shows different patterns in three distinct period ranges. At periods of 5–17 s and greater than 37 s, these regions are anisotropic. Between 17 and 37 s, however, no phase-velocity anisotropy is required by the data (the  $F$ -test values are smaller than the confidence level). Anisotropy in the southwestern Kaapvaal Craton is required at both intermediate and long periods but is less significant at short periods below 17 s.

The  $F$ -test appears to be an effective way to identify the period ranges in which the data requires azimuthal anisotropy.

## 5 AZIMUTHAL ANISOTROPY

### 5.1 Anisotropy in the four regions

The results of the inversions for Rayleigh-wave azimuthal anisotropy are displayed in Fig. 7. At the top, we show examples of data and best-fitting models at four different periods, for each of the four regions. The data (colour dots) are sorted into  $1^\circ$  bins and smoothed using a  $30^\circ$  sliding window (Section 3). The best-fitting models with the isotropic and  $2\varphi$  anisotropy parameters are shown with solid lines; models with the isotropic and both  $2\varphi$  and  $4\varphi$  anisotropy parameters are shown with dashed lines.

Anisotropy is small in most cases. The examples in Fig. 7 (top panels) show that the small amplitude of anisotropy is not an artefact due to noise or inconsistency of measurements but is clearly seen in the data. The small amplitudes are qualitatively consistent with the small *SKS*-splitting times measured in southern Africa (Fouch *et al.* 2004b; Silver *et al.* 2004).

The two frames at the bottom of Fig. 7 show the distribution of Rayleigh-wave anisotropy ( $2\varphi$ ) with period in the four regions. Accurate measurements of anisotropy must show smooth, gradual changes with period, both in their amplitudes and in their fast-propagation azimuths (unless the amplitude is close to zero). This reflects the gradual changes with period of the shapes and depth spans of the depth sensitivity kernels of Rayleigh-wave phase velocities (Fig. 4). Large anisotropy differences at adjacent periods cannot be reconciled with realistic Earth structures and indicate errors. In our models, some unrealistic variability, albeit with small

anisotropy amplitude, is seen at the shortest periods (5–10 s) in the northern and southwestern Kaapvaal Craton regions. Most of our models show gradual changes with period, as expected.

The largest anisotropy by far is seen at the short (5–10 s) periods in the Limpopo Belt, where the fast-propagation direction is approximately N–S. Rayleigh waves at these periods sample primarily the upper and middle crust (Fig. 4). In the southern Kaapvaal Craton, fast directions at periods under 10 s are also around N–S on average, although with a much smaller amplitude. In the northern Kaapvaal Craton, the crust appears to be nearly isotropic.

Intermediate periods of 15–50 s sample the lower crust and uppermost mantle (Fig. 4). At these periods, phase-velocity anisotropy is very small (under 0.5 per cent) in three (Limpopo Belt, northern Kaapvaal Craton and central Kaapvaal Craton) of the four regions.

At long periods that sample primarily the lower lithosphere (60–120 s; Fig. 4), anisotropy increases to 0.5–1.0 per cent. In all four regions, anisotropy shows nearly constant orientations across most or all of this period range. The fast-propagation directions are dissimilar in different regions: E–W in the Limpopo Belt and southwestern Kaapvaal; NE–SW in northern Kaapvaal; N–S in central Kaapvaal Craton.

At periods longer than 120–130 s, the fast-propagation directions in all regions change towards NNE–SSW. At these periods, Rayleigh-wave sensitivity depth range gradually shifts from mostly shallower to mostly deeper than 200 km, increasingly sampling the asthenosphere (Fig. 4).

### 5.2 Southern Africa average anisotropy

The change in anisotropy orientation at periods of 120–130 s is important as it appears to reflect the change of the deformation regime at the lithosphere–asthenosphere boundary. In each of the four regions, however, our inversion results at the longest periods are less robust than at periods below, due to the decrease in the amount of measurements.

We therefore merge the dispersion curves from the four subregions and invert the resulting large data set for southern Africa average anisotropy. Additional dispersion curves from longer interstation paths that cross region boundaries are added (typically, longer paths are likely to yield more long-period measurements). The combined data set consists of 5313 dispersion curves, from 646 station pairs between 133 stations (Fig. 8). The data set is inverted for region-average azimuthal anisotropy (Section 3). Fig. 9 shows fast-propagation azimuths and amplitudes of anisotropy, with examples of data-model fits at three periods.

The N–S fast directions at 5–15 s periods reflect the strong anisotropy in Limpopo Belt and, to a lesser extent, that in the southern Kaapvaal Craton, all with approximately N–S orientation. At periods that sample the lower crust and mantle lithosphere (15–100 s), the region-average anisotropy is an average over blocks with different fast directions within each (Fig. 7) and is small (Fig. 9).

At periods longer than 100–120 s, a robust, region-average, NE–SW direction of fast propagation emerges. This result confirms the approximately NE–SW fast directions yielded by region-by-region inversions, but is more robust, constrained by more data. Anisotropy at the longest periods is likely to be due to fabric in the asthenosphere (Fig. 4), created by shear associated with the current motion of the African Plate. Flow patterns in the asthenosphere can be expected to be smooth, and thus the inversion for a single fast direction beneath the entire southern Africa is meaningful.

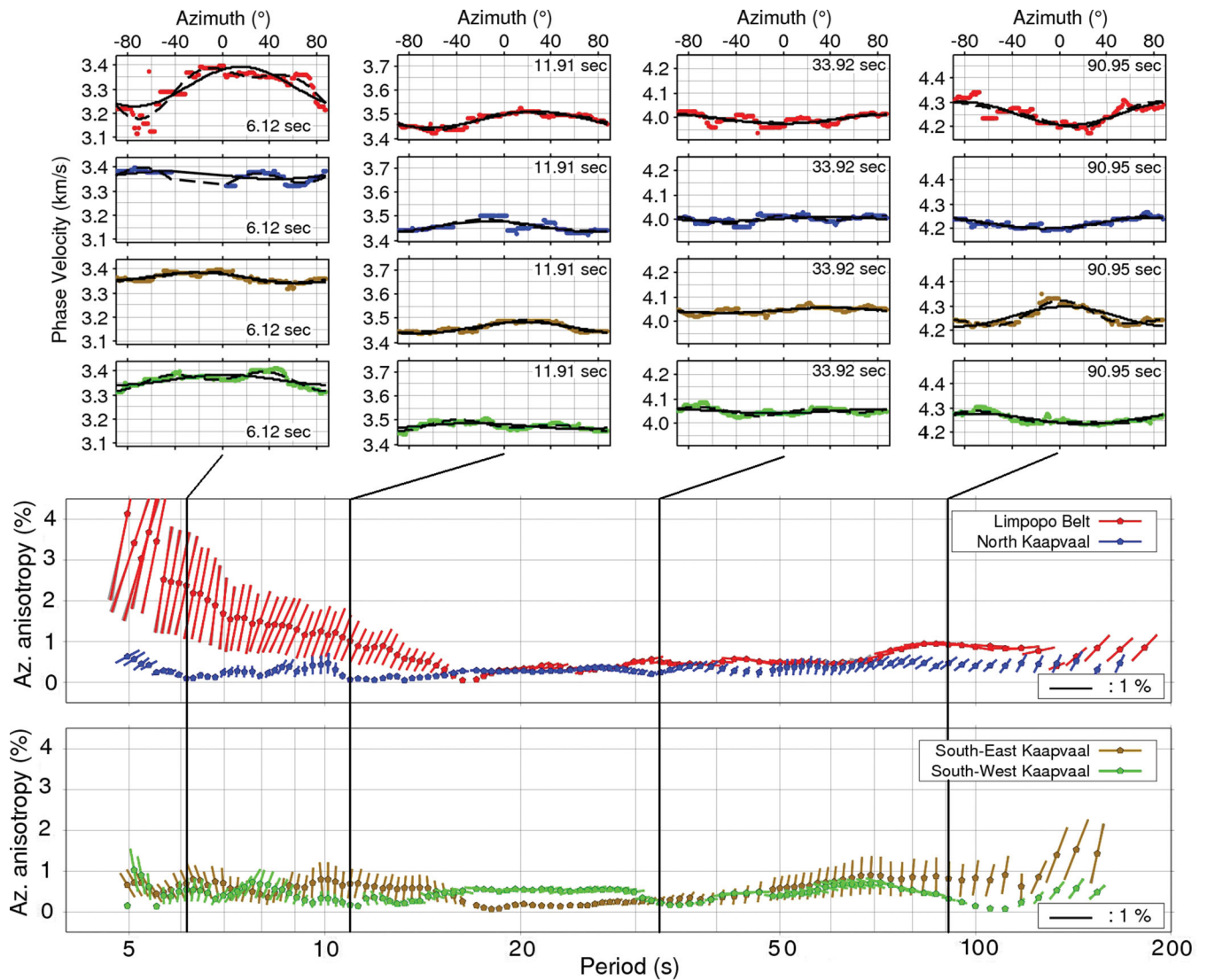


**Figure 7.** Azimuthal anisotropy in the four subregions. Top panels: examples of distributions of phase velocities with azimuths at four different periods for each subregion. Dots are the data, binned and smoothed with a  $30^\circ$  sliding window. Solid black lines: best-fitting models with isotropic and  $2\varphi$  terms. Dashed black lines: best-fitting models with isotropic,  $2\varphi$  and  $4\varphi$  terms. Bottom panels: azimuths of fast propagation and amplitude of anisotropy as a function of period for each subregion. The vertical orientation of a stick means a north–south fast-propagation azimuth; a horizontal orientation means an east–west fast-propagation azimuth.

### 5.3 An alternative inversion approach

To verify our results further, we also invert the data using an alternative approach: tomographic inversions for phase-velocity maps with anisotropy (Lebedev & van der Hilst 2008; Deschamps *et al.* 2008a). This is done for each region separately, using interstation measurements within that region only and applying very strong lateral smoothing. The smoothing represents lateral averaging over various neighbouring interstation paths. The inversions thus enhance the averaging that had been done for each station pair over the different one-event measurements available for it (Section 2). The solutions of the tomographic inverse problems (solved separately at different periods) are isotropic-average phase velocities and azimuthal anisotropy within each region. We plot the results of the inversions at a range of periods in Fig. 10. The inversions were overparametrized (the sticks that indicate the fast directions and amplitudes of anisotropy are plotted at each grid knot) but also oversmoothed, so that there are almost no variations within each

subregion. We plot anisotropy at all grid knots only to highlight the degree of model smoothness.

The results of the oversmoothed tomography are consistent with the results of our inversions for subregion-average properties (Section 3). This is to be expected, as the two inversion approaches relate the same data to the same properties of the regions, the region-average anisotropy being of primary interest. The implementation of the two inversions is quite different, however, and the close match between the results confirms their accuracy.

## 6 DISCUSSION

The dependence of phase-velocity anisotropy on period indicates the distribution of shear velocity anisotropy with depth. Although resolving the layering of anisotropy in fine detail would require an investigation of the trade-offs of various anisotropic and isotropic parameters, our phase-velocity results (Figs 7 and 9) display patterns

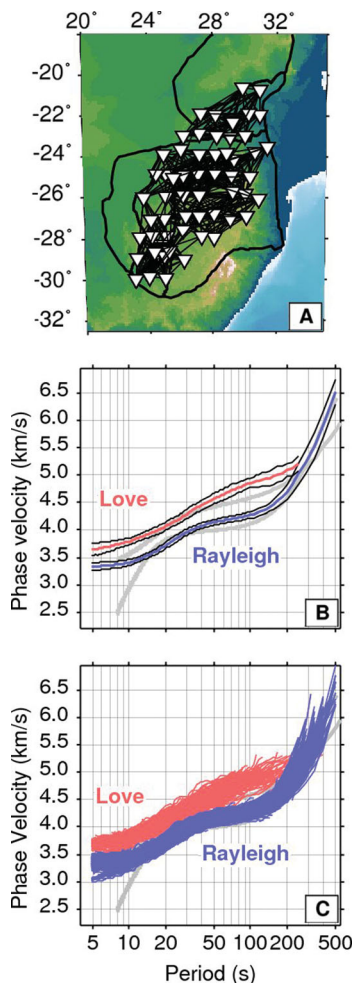


**Figure 8.** Phase-velocity measurements across the entire region. (A) Stations and stations pairs. (B) All-region-average dispersion curves for Love and Rayleigh waves. Grey: AK135 (Kennett *et al.* 1995). (C) All dispersion curves, each measured using a pair of stations and a single event.

that already reveal clearly the basic elements of the stratification of azimuthal anisotropy beneath southern Africa.

We summarize our inferences in Fig. 11 and focus on three depth ranges: the upper crust, lower-mantle lithosphere and asthenosphere. We plot average phase-velocity anisotropy across period ranges that are primarily sensitive to these depth ranges. These averages are meaningful because anisotropy patterns are clear and nearly constant within each of the period ranges, for each of our four regions (Figs 7 and 9). In contrast, phase-velocity anisotropy at periods sampling the lower crust and upper lithospheric mantle (between 10–15 and 50–70 s) is small and more variable (Fig. 7). This may reflect either the small amplitude or greater depth variability of shear velocity anisotropy in this depth range.

### 6.1 Upper crust: azimuthal anisotropy, aligned cracks, tectonic stress

The strong phase-velocity anisotropy at short periods in the Limpopo Belt indicates shear velocity anisotropy in the upper crust. This is evident from the gradual decrease in the anisotropy amplitude from 5 to 10 s period (Fig. 7), as Rayleigh waves at increasing periods sample progressively deeper crust (Fig. 4).

The N–S fast-propagation direction (Fig. 11A) is perpendicular to the E–W sutures between the Limpopo Belt and the Kaapvaal and Zimbabwe Cratons to the south and north of it. It is also perpendicular to the E–W-oriented fabric in the deep lithosphere, manifested in anisotropy we see at longer periods. It is thus unlikely to be caused by fabric imprinted into the crust during the Archean–Palaeoproterozoic deformation of the Limpopo Belt.

We conclude that the anisotropy is caused by aligned cracks. Cracks in the upper 5 km of the crust can be opened by the current tectonic stress, giving rise to strong anisotropy (e.g. Nur 1971; Crampin 1978) with fast-propagation directions parallel to the cracks and perpendicular to the extensional stress component. In eastern southern Africa, the regional stress is characterized by an E–W extension, associated with the southward propagation of the East African Rift. This stress field is documented unambiguously by the source mechanisms of numerous earthquakes, showing E–W extension (Fig. 11A).

The crack-induced anisotropy is the strongest in the Limpopo Belt probably because it is the closest to the tip of the rift. In southwestern and central Kaapvaal Craton, upper-crustal anisotropy is weaker but also with fast directions perpendicular to the regional direction of extension, evidenced by focal mechanisms (e.g. Dziewonski *et al.* 1994; Fig. 11A), and is thus likely to be due to cracks as well.

For the first time, to our knowledge, our results open the possibility of estimation of regional stress patterns from anisotropy measured using teleseismic surface waves. In southern Africa, the stress state is well known from earthquake source mechanisms. Our results suggest that in other regions around the world, where tectonic stress is poorly known, it can be estimated using broad-band array recordings of short-period surface waves, a very common data type.

### 6.2 Anisotropy in deep mantle lithosphere: record of ancient deformation

Rayleigh waves at 80–120 s sample primarily the lower-mantle lithosphere (100–200 km depths; Fig. 4) and show an E–W fast-propagation direction beneath the Limpopo Belt (Fig. 11B). Beneath the neighbouring northern Kaapvaal Craton, the average fast-propagation direction is similar, ENE–WSW. These fast directions are parallel to the sutures associated with the Archean and Palaeoproterozoic orogenies in which what is now the northern Kaapvaal Craton and Limpopo Belt accreted to the Kaapvaal Craton's core (De Wit *et al.* 1992; Roering *et al.* 1992; Kamber *et al.* 1995; Holzer *et al.* 1998; Silver *et al.* 2004). The suture of the Limpopo Belt with the Zimbabwe Craton to the north is also late Archean or Palaeoproterozoic and also strikes approximately E–W. The anisotropy is likely to indicate suture-parallel fabric which is a record of the ancient deformation of the deep lithosphere.

The western Kaapvaal Craton (the Kimberly Block) also joined the Kaapvaal Craton's core in the late Archean, with the suture between the two now oriented N–S. Western Kaapvaal's lower-lithosphere anisotropy, however, does not show a fast-propagation direction parallel to the suture; it is oriented nearly perpendicular to it. This suggests that the continental collision of the western and central blocks of the Kaapvaal Craton was accommodated by a different mechanism compared to the collisions in the north. The entire lithosphere of the Limpopo and northern Kaapvaal blocks has undergone pervasive deformation, as evidenced by the suture-parallel fabric frozen into it. In contrast, the lithosphere of the western

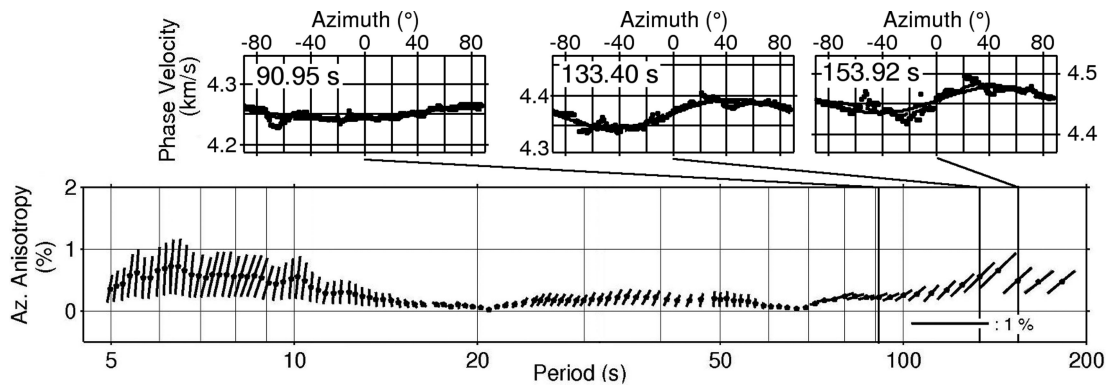


**Figure 9.** All-region-average azimuthal anisotropy. Top panels: example distributions of phase velocities with azimuths at three different periods (the long periods is where all-region-average anisotropy is most meaningful). Dots are the data, binned and smoothed using a  $30^\circ$  sliding window. Solid black lines: best-fitting models with isotropic and  $2\varphi$  terms. Dashed black lines: best-fitting models with isotropic,  $2\varphi$  and  $4\varphi$  terms. Bottom panels: the azimuth of fast propagation and amplitude of anisotropy as a function of period. The vertical orientation of a stick means north–south, and horizontal orientation means east–west fast-propagation azimuth.

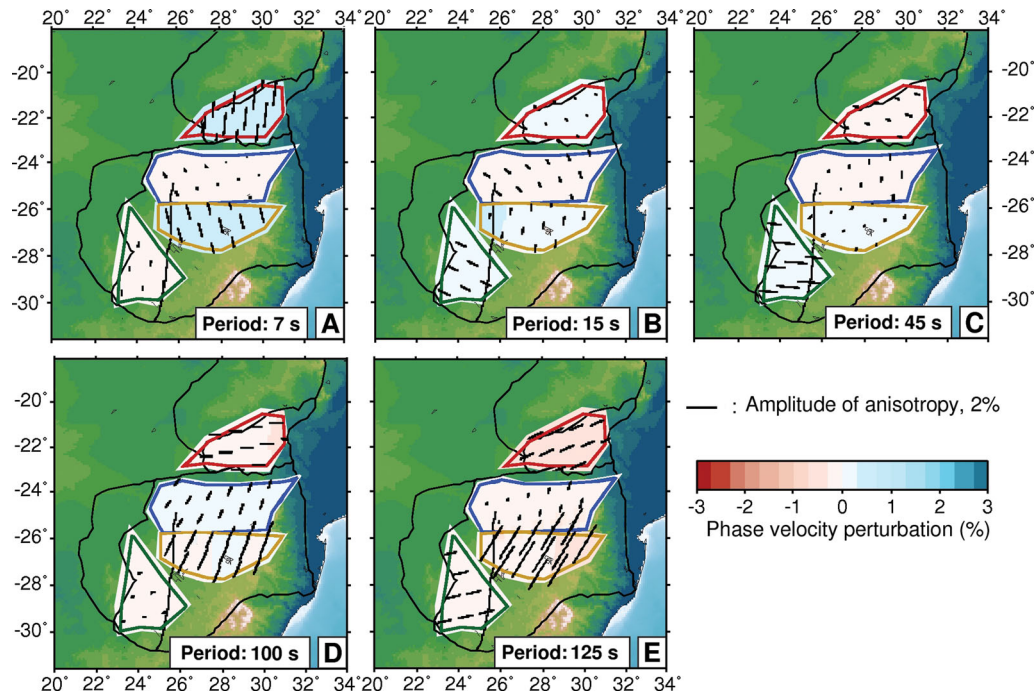


**Figure 10.** Strongly smoothed phase-velocity tomography at five different periods. Separate inversions are performed for each region, with the results then plotted on the same maps for compactness. Sticks indicate directions of fast propagation. Isotropic phase-velocity anomalies (colour scale) are with respect to the averages over the entire region (Fig. 8).

Kaapvaal Craton shows fabric oriented perpendicular to the suture. This may indicate that the Kimberly Block was stronger at the time of the collision, or, alternatively, that it was not subjected to compression or transpression as the northern Kaapvaal and Limpopo blocks were.

### 6.3 Anisotropy in the asthenosphere: current flow

At periods longer than 120–130 s (Fig. 4), Rayleigh waves sample primarily below 200 km depth. At these periods, anisotropy in all subregions aligns approximately with the NE–SW motion of the African Plate (Fig. 11C). The match is confirmed by the inversions of all available data for all-region-average anisotropy, yielding ro-

bust, NE–SW fast-propagation directions at long periods (Fig. 11C, grey bars).

The long-period anisotropy thus indicates fabric in the asthenosphere, created by the shear associated with the current plate motion. Azimuthal anisotropy aligned with the plate motion has been detected previously beneath other cratons, including those in Australia (e.g. Debayle *et al.* 2005) and North America (Snyder & Brunton 2007; Deschamps *et al.* 2008b; Darbyshire & Lebedev 2009; Yuan & Romanowicz 2010). In the Kaapvaal Craton, many of the deepest-sampling xenoliths show a sheared texture, which may be evidence of asthenospheric flow fabric (e.g. James *et al.* 2004). Our results confirm that plate motions produce detectable anisotropic fabric within the asthenosphere beneath cratons.

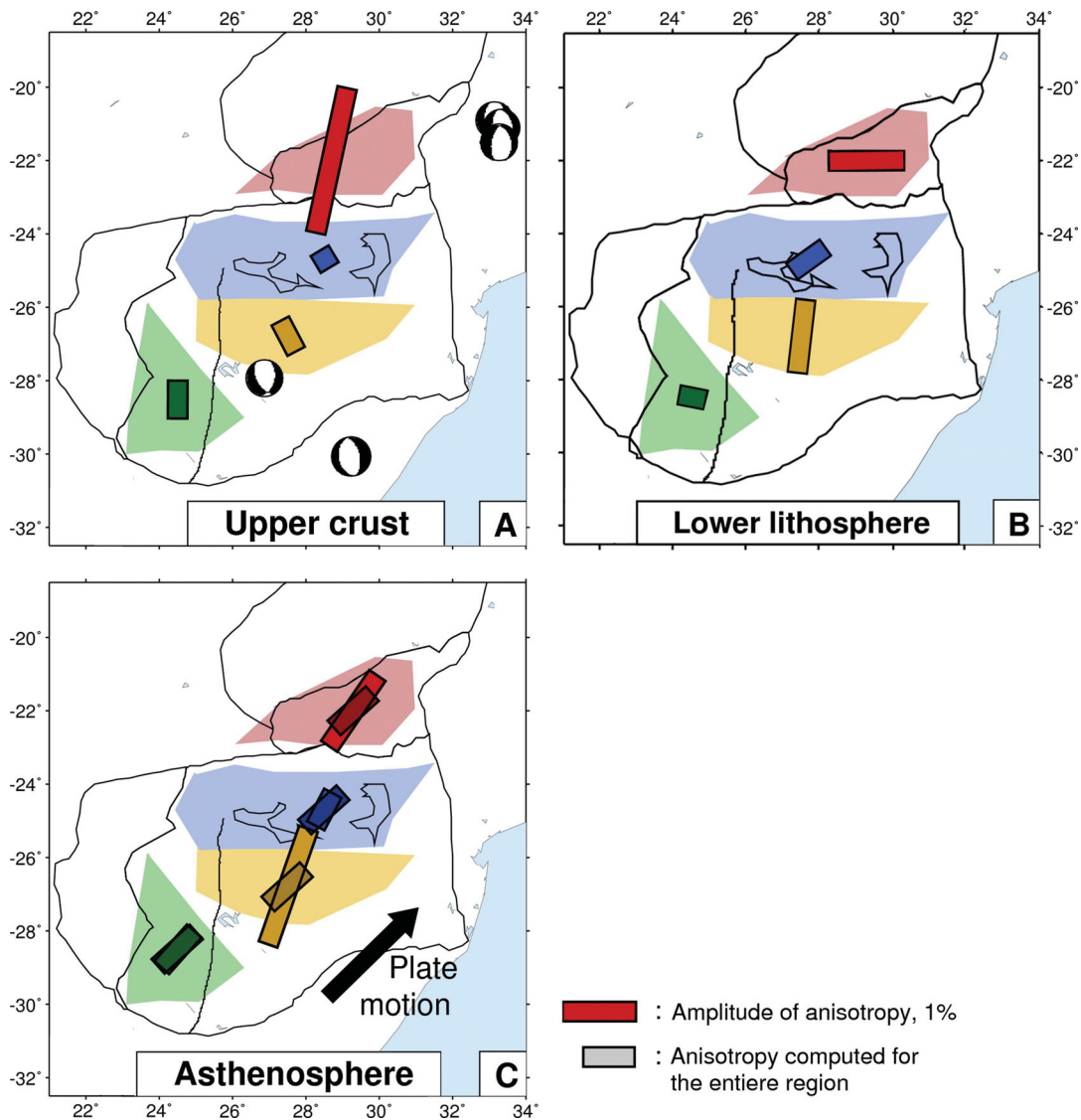


**Figure 11.** Azimuthal anisotropy of Rayleigh waves sampling primarily the upper crust (A), lower lithosphere (B) and asthenosphere (C). (A) Fast-propagation directions of Rayleigh waves at 5–7 s periods. Focal mechanisms of earthquakes are plotted to indicate the regional tectonic stress (e.g. Dziewonski *et al.* 1994). (B) Fast-propagation directions at 80–120 s periods, with sensitivity primarily to the deep mantle lithosphere. (C) Fast-propagation directions at 130–160 s periods, with sensitivity primarily below 200 km. The plate motion direction is from Gripp & Gordon (1990). Grey bars: fast directions from the inversion for all-region-average anisotropy.

Evans *et al.* (2011) investigated the electrical resistivity structure of the Kaapvaal Craton and reported indications for electrical anisotropy near the lithosphere–asthenosphere boundary, with higher conductivities in a direction parallel to the plate motion. This could be interpreted as evidence for plate-motion parallel flow, although Evans *et al.* (2011) noted that the anisotropy was not quite statistically significant. In an earlier study, Hamilton *et al.* (2006) found highly variable orientations of apparent electrical anisotropy in the crust and lithospheric mantle, which, however, was likely to be due to a combination of factors, including isotropic heterogeneity.

#### 6.4 Origin of SKS-splitting beneath southern Africa

Previous SKS-splitting measurements in southern Africa (Fig. 12) prompted two different, end-member interpretations, with impor-

tant implications regarding the deformation of the lithosphere and asthenosphere. According to one interpretation (Vinnik *et al.* 1995), anisotropy is present in the asthenosphere, reflecting the shear associated with the plate motion, while frozen anisotropy in the ancient lithosphere may also occur but is not dominant. According to the other interpretation (Silver *et al.* 2004), anisotropy is present in the lithosphere and is weak or absent in the asthenosphere, with the implication that fast-propagation directions inferred from SKS splitting show the orientation of fabric within the lithosphere. This allowed the inference that late-Archean–Palaeoproterozoic orogenies in southern Africa were accommodated by pervasive suture-parallel flow in the mantle lithosphere of both the Kimberly and Pietersburg blocks, now in the western and northern parts of the Kaapvaal Craton, respectively, as well as in the lithosphere of the Limpopo Belt to the north. This ancient deformation thus created anisotropic fabric that remains frozen within the deep lithosphere until present.

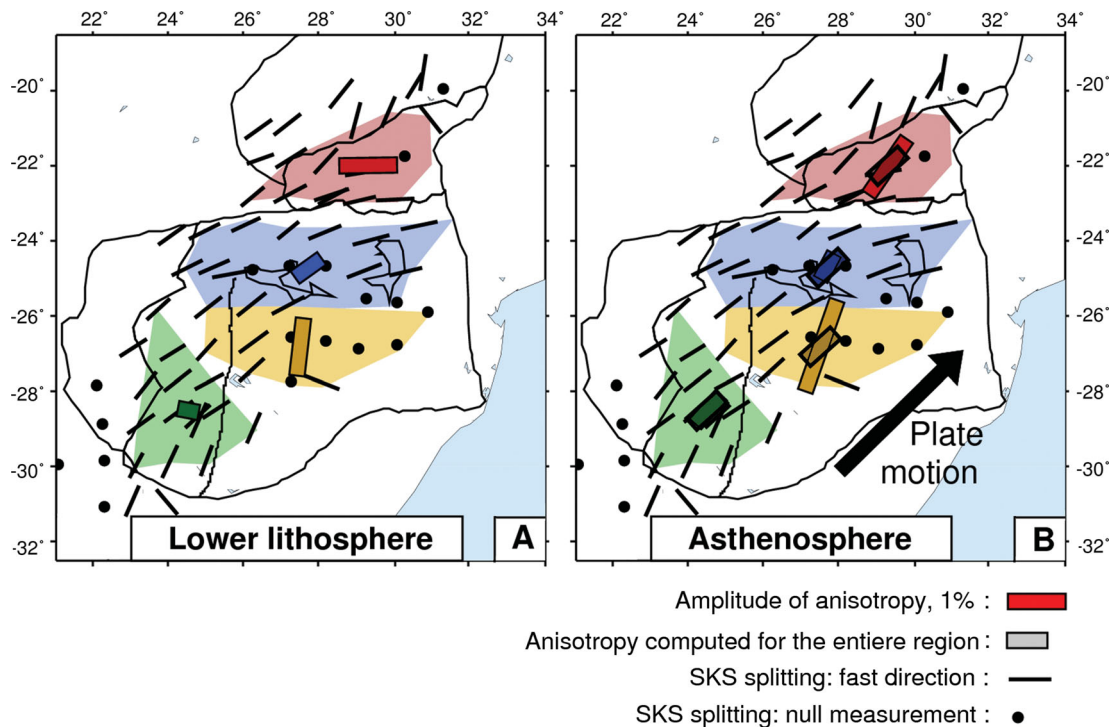


**Figure 12.** Origin of *SKS*-splitting: a comparison of azimuthal anisotropy in the lithosphere and asthenosphere and the fast directions inferred from *SKS*-splitting. (A) Fast-propagation directions at 80–120 s periods, with sensitivity primarily to the deep mantle lithosphere, compared to the fast directions from *SKS*-splitting (black; Silver *et al.* 2004). (B) Fast-propagation directions at 130–160 s periods, with sensitivity primarily below 200 km (asthenosphere), compared to the fast directions from *SKS*-splitting. The plate motion direction is from Gripp & Gordon (1990).

Our results provide the vertical resolution that the *SKS* measurements lack. They show (Fig. 12) that the distribution of anisotropy beneath southern Africa comprises elements of both end-member models. Beneath the northern Kaapvaal Craton and Limpopo Belt, the E–W to ENE–WSW fast-propagation directions inferred from *SKS* splitting match those within the deep mantle lithosphere (Fig. 12A) and not those within the asthenosphere (Fig. 12B). This shows that *SKS* splitting originates within the lithosphere and confirms that the entire lithosphere is likely to have been reworked in the Archean–Palaeoproterozoic orogenies (De Wit *et al.* 1992; Roering *et al.* 1992; Kamber *et al.* 1995; Holzer *et al.* 1998; Silver *et al.* 2004) undergoing suture-parallel flow, in agreement with the interpretation of Silver *et al.* (2004).

In the Kimberly Block in western Kaapvaal Craton, in contrast, fast-propagation directions inferred from *SKS* splitting do not match those within the mantle lithosphere (Fig. 12A) but, instead, match fast-propagation directions within the asthenosphere (Fig. 12B). *SKS* splitting in western Kaapvaal is thus likely to originate primarily in the asthenosphere and reflects the present plate-motion related flow within it, as suggested by Vinnik *et al.* (1995). The lack of suture-parallel fabric within the lithosphere of the Kimberly block suggests that it was not reworked when it joined the Kaapvaal Craton, unlike the blocks that accreted in the north. This may have been either due to the mechanical strength of this block or because the collision mechanism was different from that in the north.

Small-scale variations in the amplitude of *SKS*-splitting near Kimberley observed by Fouch *et al.* (2004b) are likely to reflect small-scale variations in anisotropy within the lithosphere. Our results represent average anisotropy over relatively large blocks within the Kaapvaal Craton and should be compared to the smooth,

regional-scale spatial patterns shown by *SKS*-splitting measurements (Fig. 11).

Note added in revision: in a just-published study, Vinnik *et al.* (2012) report their joint analysis of *P*-receiver functions and *SKS*-splitting at 23 SASE stations within and around the Limpopo Belt. They conclude that the E–W anisotropic fabric within the belt's lithosphere is underlain by a NE–SW orientated fabric within the asthenosphere. The close agreement of their results with our results for this part of southern Africa further confirms the occurrence of stratified azimuthal anisotropy.

## 7 CONCLUSIONS

We have measured phase velocities of surface waves between pairs of SASE stations in southern Africa. For four subregions (the northern, central and southwestern Kaapvaal Craton and the Limpopo Belt), with relatively homogeneous structure within each, we derived robust, Rayleigh- and Love-wave, region-average dispersion curves in a very broad period range: from 5 to 250–400 s (Rayleigh) and from 5 to 100–250 s (Love), depending on the region.

Surface wave anisotropy indicates the distribution of azimuthal anisotropy with depth in the different parts of southern Africa. Our azimuthal coverage was sufficient to determine Rayleigh-wave anisotropy within each region at periods from 5 to 150–200 s, resolving anisotropy from the upper crust down to the asthenosphere.

We used the jackknife method to estimate uncertainties and the *F*-test to determine whether or not anisotropy was required by the data. The *F*-test results confirmed that  $2\phi$  anisotropy was required between 5 and 17 s and at periods greater than 35 s. No phase-velocity azimuthal anisotropy was required by the data between 17

and 35 s in three out of four regions.  $4\varphi$  anisotropy was also inverted for but was found to be small and not statistically significant in almost all cases.

Strong anisotropy measured in the Limpopo Belt at short periods (5–10 s, decreasing with period) is probably due to aligned microcracks. The regional E–W extensional stress, associated with the South-ward propagation of the East African Rift, is evident from earthquake source mechanisms and is likely to have opened N–S-oriented cracks. This matches the N–S fast Rayleigh-wave propagation directions that we detect both in the Limpopo Belt and, with a smaller amplitude, in the central and western Kaapvaal Craton. Our results show that it is possible to estimate regional stress from surface-wave anisotropy, measured using broad-band array recordings of short-period surface waves.

Fabric within the deep mantle lithosphere of the Limpopo Belt and northern Kaapvaal Craton is aligned E–W to ENE–WSW, parallel to the Archean–Palaeoproterozoic sutures where these blocks got attached to the core of the craton and to each other. Our results confirm the earlier inferences made by Silver *et al.* (2004) from their *SKS*-splitting measurements: (i) that the entire lithosphere of these blocks underwent pervasive deformation with suture-parallel flow during the ancient continental collisions, and (ii) that the fabric created by the Archean–Palaeoproterozoic deformation is preserved within the lithosphere to this day. Suture-parallel fabric is absent in the deep lithosphere of the western Kaapvaal Craton (Kimberly block). It was not, therefore, reworked in the collision with the central Kaapvaal Craton, unlike the blocks that accreted in the north. This may have been either due to its mechanical strength or because the collision mechanism was different from those that operated in the north. The depth resolution of the surface wave data also provides a solution to the debate over the interpretation of *SKS*-splitting measurements: asthenospheric (Vinnik *et al.* 1995) versus lithospheric (Silver *et al.* 2004) dominant anisotropy. The distribution of anisotropy beneath southern Africa comprises elements of both models. Anisotropy in the asthenosphere is present and shows fast directions parallel to the plate motion, as argued by Vinnik *et al.* (2004). Anisotropy in the Limpopo and northern Kaapvaal Craton lithosphere shows fast directions parallel to the Archean–Palaeoproterozoic sutures, as suggested by Silver *et al.* (2004). The depth intervals where the *SKS* splitting originates can be determined by comparing the depth distributions of anisotropy and the fast directions given by the splitting measurements. Beneath the Limpopo Belt and northern Kaapvaal Craton, *SKS* splitting reflects the E–W- and ENE–WSW-oriented fabric in the lithosphere, as argued by Silver *et al.* (2004). Beneath the western Kaapvaal Craton, in contrast, *SKS* splitting reflects the fabric in the asthenosphere, oriented parallel to the SW–NE plate motion, as argued by Vinnik *et al.* (1995).

## ACKNOWLEDGMENTS

The authors would like to thank Jeannot Trampert and Balz Kamber for insightful discussions on misfit statistics and on tectonic evolution of the Limpopo Belt, and Derek Schutt, an anonymous reviewer and the Editor, Gabi Laske, for helpful comments on the manuscript. They are grateful to the Kaapvaal Project seismic team for collecting the data. The facilities of the IRIS Data Management System, and specifically the IRIS Data Management Center, were used for access to waveform and metadata used in this study. Figures were generated with Generic Mapping Tools (Wessel & Smith 1995). This work was funded by the Dublin Institute for Ad-

vanced Study and, in part, by Science Foundation Ireland (grants 08/RFP/GEO1704 and 09/RFP/GEO2550).

## REFERENCES

- Adams, A. & Nyblade, A., 2011. Shear wave velocity structure of the southern African upper mantle with implications for the uplift of southern Africa, *Geophys. J. Int.*, **186**, 808–824, doi:10.1111/j.1365-246X.2011.05072.x.
- Becker, T.W., Chevrot, S., Schulte-Pelkum, V. & Blackman, D.K., 2006. Statistical properties of seismic anisotropy predicted by upper mantle geodynamic models, *J. geophys. Res.*, **111**, B08309, doi:10.1029/2005JB004095.
- Becker, T.W., Lebedev, S. & Long, M.D., 2012. On the relationship between azimuthal anisotropy from shear wave splitting and surface wave tomography, *J. geophys. Res.*, **117**, B01306, doi:10.1029/2011JB008705.
- Begg, G. *et al.*, 2009. The lithospheric architecture of Africa: seismic tomography, mantle petrology and tectonic evolution, *Geosphere*, **5**, 23–50.
- Beghein, C., Snoko, J.A. & Fouch, M.J., 2010. Depth constraints on azimuthal anisotropy in the Great Basin from Rayleigh wave phase velocity maps, *Earth planet. Sci. Lett.*, **289**, 467–478.
- Bevington, P.R., 1969. *Data Reduction and Error Analysis for the Physical Sciences*, McGraw-Hill, New York, NY.
- Bodin, T. & Maupin, V., 2008. Resolution potential of surface wave phase velocity measurements at small arrays, *Geophys. J. Int.*, **172**, 698–706.
- Bolton, H., Hutt, C.R., Slad, G. & Woodward, R.L., 1998. *Bulletin on Timing Issues with GSN Data July 27, 1998*, Albuquerque Seismological Laboratory, Data Collection Center, <http://earthquake.usgs.gov/regional/asl/data/timing.php>
- Carlson, R.W., Grove, T.L., de Wit, M.J. & Gurney, J.J., 1996. Anatomy of an Archean craton: a program for interdisciplinary studies of the Kaapvaal craton, southern Africa, *EOS, Trans. Am. geophys. Un.*, **77**, 273–277.
- Carlson, R.W., Pearson, D.G., Boyd, F.R., Shirey, S.B., Irvine, G., Menzies, A.H. & Gurney, J.J., 1999. Re-Os systematics of lithospheric peridotites: implications for lithosphere formation and preservation, in *Proceedings of 7th International Kimberlite Conference*, Cape Town, South Africa, pp. 99–108.
- Carlson, R.W. *et al.*, 2000. Continental growth, preservation and modification in southern Africa, *GSA Today*, **10**, 1–7.
- Chevrot, S. & Zhao, L., 2007. Multiscale finite-frequency Rayleigh wave tomography of the Kaapvaal craton, *Geophys. J. Int.*, **169**, 201–215.
- Crampin, S., 1978. Seismic wave propagation through a cracked solid: polarization as a possible dilatancy diagnostic, *Geophys. J. R. astr. Soc.*, **53**, 467–496.
- Darbyshire, F.A. & Lebedev, S., 2009. Rayleigh wave phase-velocity heterogeneity and multilayered azimuthal anisotropy of the Superior Craton, Ontario, *Geophys. J. Int.*, **176**, 215–234.
- De Wit, M.J. *et al.*, 1992. Formation of an Archean continent, *Nature*, **357**, 553–562.
- Debayle, E., Kennett, B.N.L. & Priestley, K., 2005. Global azimuthal seismic anisotropy and the unique plate-motion deformation of Australia, *Nature*, **433**, 509–512.
- Deschamps, F., Lebedev, S., Meier, T. & Trampert, J., 2008a. Azimuthal anisotropy of Rayleigh-wave phase velocities in the east-central United States, *Geophys. J. Int.*, **173**, 827–843.
- Deschamps, F., Lebedev, S., Meier, T. & Trampert, J., 2008b. Stratified seismic anisotropy reveals past and present deformation beneath the East-Central United States, *Earth planet. Sci. Lett.*, **274**, 489–498.
- Dziewonski, A.M. & Anderson, D.L., 1981. Preliminary reference Earth model, *Phys. Earth planet. Int.*, **25(4)**, 297–356.
- Dziewonski, A.M., Ekström, G. & Salganik, M.P., 1994. Centroid-moment tensor solutions for January–March 1994, *Phys. Earth planet. Inter.*, **86**, 253–261.
- Efron, B. & Tibshirani, R., 1986. Bootstrap methods for standard errors, confidence intervals, and other measures of statistical accuracy, *Statistical Science*, **1**, 54–75.

- Eglington, B.M. & Armstrong, R.A., 2004. The Kaapvaal craton and adjacent orogens, southern Africa: a geochronological database and overview of the geological development of the craton, *South Afr. J. Geol.*, **107**, 13–32.
- Endrun, B., Meier, T., Lebedev, S., Bohnhoff, M., Stavarakakis, G. & Harjes, H.P., 2008. S velocity structure and radial anisotropy in the Aegean region from surface wave dispersion, *Geophys. J. Int.*, **174**, 593–616.
- Endrun, B., Lebedev, S., Meier, T., Tirel, C. & Freiderich, W., 2011. Complex layered deformation within the Aegean crust and mantle revealed by seismic anisotropy, *Nature Geosci.*, **4**, 203–207.
- Evans, R.L. *et al.*, 2011. Electrical lithosphere beneath the Kaapvaal craton, southern Africa, *J. geophys. Res.*, **116**, B04105, doi:10.1029/2010JB007883.
- Fishwick, S., 2010. Surface wave tomography: imaging of the lithosphere-asthenosphere boundary beneath central and southern Africa, *Lithos*, **120**, 63–73.
- Fishwick, S. & Bastow, I.R., 2011. Towards a better understanding of African topography: a review of passive-source seismic studies of the African crust and upper mantle, in *The Formation and Evolution of Africa: A Synopsis of 3.8 Ga of Earth History*, Geol. Soc. London, Spec. Publ. Vol. 357, pp. 343–371, eds van Hinsbergen, D.J.J., Buiter, S.J.H., Torsvik, T.H., Gaina, C. & Webb, S.J., Geological Society, London.
- Foster, A.N. & Jackson, J.A., 1998. Source parameters of large African earthquakes: implications for crustal rheology and regional kinematics, *Geophys. J. Int.*, **134**, 422–448.
- Fouch, M.J., James, D.E., van der Car, J.C., van der Lee, S. & The Kaapvaal Seismic Group, 2004a. Mantle seismic structure beneath the Kaapvaal and Zimbabwe cratons, *South Afr. J. Geol.*, **107**, 33–44.
- Fouch, M.J., Silver, P.G., Bell, D.R. & Lee, J.N., 2004b. Small-scale variations in seismic anisotropy near Kimberley, South Africa, *Geophys. J. Int.*, **157**, 764–774.
- Freybourger, M., Gaherty, J.B., Jordan, T.H. & the Kaapvaal Seismic Group, 2001. Structure of the Kaapvaal craton from surface waves, *Geophys. Res. Lett.*, **28**, 2489–2492.
- Friederich, W., Hunzinger, S. & Wielandt, E., 2000. A note on the interpretation of seismic surface waves over three-dimensional structures, *Geophys. J. Int.*, **143**, 335–339.
- Fry, B., Deschamps, F., Kissling, E., Stehly, L. & Giardini, D., 2010. Layered azimuthal anisotropy of Rayleigh wave phase velocities in the European Alpine lithosphere inferred from ambient noise, *Earth planet. Sci. Lett.*, **297**(1/2), 95–102.
- Fullea, J., Muller, M.R. & Jones, A.G., 2011. Electrical conductivity of continental lithospheric mantle from integrated geophysical and petrological modelling: application to the Kaapvaal Craton and Rehoboth Terrane, southern Africa, *J. geophys. Res.*, **116**, B10202, doi:10.1029/2011JB008544.
- Fullea, J., Lebedev, S., Agius, M.R., Jones, A.G. & Afonso, J.C., 2012. Lithospheric structure in the Baikal-central Mongolia region from integrated geophysical-petrological inversion of surface-wave data and topographic elevation, *Geochem. Geophys. Geosyst.*, doi:10.1029/2012GC004138, in press.
- Good, N. & De Wit, M.J., 1997. The Thabazimbi-Murchison lineament of the Kaapvaal Craton, South Africa: 2700 Ma of episodic deformation, *J. geol. Soc., Lond.*, **154**, 93–97.
- Griffin, W.L., Graham, S., O'Reilly, S.Y. & Pearson, N.J., 2004. Lithosphere evolution beneath the Kaapvaal Craton: Re-Os systematics of sulfides in mantle-derived peridotites, *Chem. Geol.*, **208**, 89–118.
- Gripp, A.E. & Gordon, R.G., 1990. Current plate velocities relative to the hotspots incorporating the NUVEL-1 global plate motion model, *Geophys. Res. Lett.*, **17**, 1109–1112.
- Hamilton, M. *et al.*, 2006. Electrical anisotropy of South African lithosphere compared with seismic anisotropy from shear-wave splitting analyses. *Phys. Earth planet. Inter.*, **158**, 226–239.
- Holzer, L., Frei, R., Barton, J.M., Jr., & Kramers, J.R., 1998. Unraveling the record of successive high grade events in the central zone of the Limpopo belt using Pb single phase dating of metamorphic minerals. *Precambrian Res.*, **87**, 87–115.
- Irvine, G.J., Pearson, D.G. & Carlson, R.W., 2001. Lithospheric mantle evolution of the Kaapvaal Craton: a Re-Os isotope study of peridotite xenoliths from Lesotho kimberlites, *Geophys. Res. Lett.*, **28**, 2505–2508.
- James, D.E., Fouch, M.J., van der Car, J.C., van der Lee, S. & the Kaapvaal group, 2001. Tectospheric structure beneath southern Africa, *Geophys. Res. Lett.*, **13**, 2485–2488.
- James, D.E., Boyd, F.R., Schutt, D., Bell, D.R. & Carlson, R.W., 2004. Xenolith constraints on seismic velocities in the upper mantle beneath southern Africa, *Geochem. Geophys. Geosyst.*, **5**, Q01002, doi:10.1029/2003GC000551.
- Jordan, T.H., 1975. The continental tectosphere, *Rev. Geophys.*, **13**, 1–12.
- Jordan, T.H., 1988. Structure and formation of the continental tectosphere, *J. Petrol., Special Volume*, **1**, 11–37.
- Kamber, B.S., Kramers, J.D., Napier, R., Cliff, R.A. & Rollinson, H.R., 1995. The Triangle Shearzone, Zimbabwe, revisited: new data document an important event at 2.0 Ga in the Limpopo Belt, *Precambrian Res.*, **70**, 191–213.
- Kennett, B.L.N., Engdahl, E.R. & Buland, R., 1995. Constraints on seismic velocities in the Earth from traveltimes, *Geophys. J. Int.*, **122**, 108–124.
- Kgaswane, E.M., Nyblade, A.A., Julia, J., Dirks, P.H.G.M., Durrheim R.J. & Pasyanos, M.E., 2009. Shear wave velocity structure of the lower crust in southern Africa: evidence for compositional heterogeneity within archaean and proterozoic terrains. *J. geophys. Res.*, **114**, B12304, doi:10.1029/2008JB006217.
- Khan, A., Boschi, L. & Connolly, J.A.D., 2011. Mapping the Earth's thermochemical and anisotropic structure using global surface wave data. *J. geophys. Res.*, **116**(B1), B01301, doi:10.1029/2010JB007828.
- Kwabida, M.T.O.G., Wright, C., Kgaswane, E.M., Simon, R.E. & Nguuri, T.K., 2003. Pn arrivals and lateral variations of Moho geometry beneath the Kaapvaal craton, *Lithos*, **71**, 393–411.
- Lebedev, S. & van der Hilst, R.D., 2008. Global upper-mantle tomography with the automated multimode inversion of surface and S-wave forms, *Geophys. J. Int.*, **173**, 505–518.
- Lebedev, S., Nolet, G., Meier, T. & van der Hilst, R.D., 2005. Automated multimode inversion of surface and S waveforms, *Geophys. J. Int.*, **162**, 951–964.
- Lebedev, S., Meier, T. & van der Hilst, R.D., 2006. Asthenospheric flow and origin of volcanism in the Baikal Rift area, *Earth planet. Sci. Lett.*, **249**, 415–424.
- Lebedev, S., Boonen, J. & Trampert, J., 2009. Seismic structure of Precambrian lithosphere: new constraints from broadband surface-wave dispersion, *Lithos*, **109**, 96–111.
- Li, A., 2011. Shear wave model of southern Africa from regional Rayleigh wave tomography with 2-D sensitivity kernels, *Geophys. J. Int.*, **185**, 832–844.
- Li, A. & Burke, K., 2006. Upper mantle structure of southern Africa from Rayleigh wave tomography, *J. geophys. Res.*, **111**, doi:10.1029/2006JB004321.
- Lin, F.C., Ritzwoller, M.H., Yang, Y., Moschetti, M.P. & Fouch, M.J., 2011. Complex and variable crustal and uppermost mantle seismic anisotropy in the western United States, *Nature Geosci.*, **4**, 55–61.
- Long, M.D. & Becker, T.W., 2010. Mantle dynamics and seismic anisotropy, *Earth planet. Sci. Lett.*, **297**, 341–354.
- Meier, T., Dietrich, K., Stöckhert, B. & Harjes, H.P., 2004. One-dimensional models of shear wave velocity for the eastern Mediterranean obtained from the inversion of Rayleigh wave phase velocities and tectonic implications, *Geophys. J. Int.*, **156**, 45–58.
- Montagner, J. & Tanimoto, T., 1991. Global upper mantle tomography of seismic velocities and anisotropies, *J. geophys. Res.*, **96**, 20 337–20 351.
- Moser, D.E., Flowers, R.M. & Hart, R.J., 2001. Birth of the Kaapvaal tectosphere 3.08 billion years ago, *Science*, **291**, 465–468.
- Muller, M.R. *et al.*, 2009. Lithospheric structure, evolution and diamond prospectivity of the Rehoboth Terrane and western Kaapvaal Craton, southern Africa: constraints from broadband magnetotellurics, *Lithos*, **112**, 93–105, doi:10.1016/j.lithos.2009.06.023.
- Nair, S.K., Gao, S.S., Liu, K.H. & Silver, P.G., 2006. Southern African crustal evolution and composition: constraints from receiver function studies, *J. geophys. Res.*, **111**, doi:10.1029/2005JB003802.

Nguuri, T.K. *et al.*, 2001. Crustal structure beneath southern Africa and its implications for the formation and evolution of the Kaapvaal and Zimbabwe cratons, *Geophys. Res. Lett.*, **28**, 2501–2504.

Nur, A., 1971. Effects of stress on velocity anisotropy in rocks with cracks, *J. geophys. Res.*, **76**, 2022–2034.

Pearson, D.G., Carlson, R.W., Shirey, S.B., Boyd, F.R. & Nixon, P.H., 1995. Stabilisation of Archean lithospheric mantle: a Re-Os isotope study of peridotite xenoliths from the Kaapvaal craton, *Earth planet. Sci. Lett.*, **134**, 341–357.

Pedersen, H.A., 2006. Impacts of non-plane waves on two-station measurements of phase velocities, *Geophys. J. Int.*, **165**, 279–287.

Pedersen, H.A., Bruneton, M., Maupin, V. & SVEKALAPKO Seismic Tomography Working Group, 2006. Lithospheric and sublithospheric anisotropy beneath the Baltic Shield from surface-wave array analysis, *Earth planet. Sci. Lett.*, **244**, 590–605.

Polat, G., Lebedev, S., Readman, P.W., O'Reilly, B.M. & Hauser, F., 2012. Anisotropic Rayleigh-wave tomography of Ireland's crust: implications for crustal accretion and evolution within the Caledonian Orogen, *Geophys. Res. Lett.*, **39**, L04302, doi:10.1029/2012GL051014.

Priestley, K., 1999. Velocity structure of the continental upper mantle: evidence from southern Africa. *Lithos*, **48**, 45–56.

Priestley, K. & Tilmann, F., 2009. Relationship between the upper mantle high velocity seismic lid and the continental lithosphere, *Lithos*, **109**, 112–124.

Priestley, K., McKenzie, D. & Debayle, E., 2006. The state of the upper mantle beneath southern Africa. *Tectonophysics*, **416**, 101–112.

Roering, C. *et al.*, 1992. Tectonic model for the evolution of the Limpopo Belt, *Precambrian Res.*, **55**, 539–552.

Saltzer, R.L., 2002. Upper mantle structure of the Kaapvaal craton from surface wave analysis: a second look, *Geophys. Res. Lett.*, **29**(6), doi:10.1029/2001GL013702.

Savage, M.K., 1999. Seismic anisotropy and mantle deformation: what have we learned from shear wave splitting? *Rev. Geophys.*, **37**, 65–106.

Schmitz, M.D., Bowring, S.A., de Wit, M.J. & Gartz, V., 2004. Subduction and terrane collision stabilize the western Kaapvaal craton tectosphere 2.9 billion years ago, *Earth planet. Sci. Lett.*, **222**, 363–376.

Schutt, D.L. & Lesher, C.E., 2010. Compositional trends among Kaapvaal Craton garnet peridotite xenoliths and their effects on seismic velocity and density, *Earth planet. Sci. Lett.*, **300**, 367–373.

Silver, P.G., 1996. Seismic anisotropy beneath the continents: probing the depths of geology, *Annu. Rev. Earth planet. Sci.*, **24**, 385–432.

Silver, P.G., Gao, S.S., Liu, K.H. & the Kaapvaal group, 2001. Mantle deformation beneath southern Africa. *Geophys. Res. Lett.*, **28**, 2493–2496.

Silver, P.G., Fouch, M.J., Gao, S.S., Schmitz, M. & the Kaapvaal Seismic Group, 2004. Seismic anisotropy, mantle fabric and the magmatic evolution of Precambrian southern Africa, *South Afr. J. Geol.*, **107**, 45–48.

Simons, F.J., van der Hilst, R.D., Montagner, J. & Zielhuis, A., 2002. Multi-mode Rayleigh wave inversion for heterogeneity and azimuthal anisotropy of the Australian upper mantle, *Geophys. J. Int.*, **151**, 738–754.

Smith, M.L. & Dahlen, F.A., 1973. The azimuthal dependence of Love and Rayleigh wave propagation in a slightly anisotropic medium, *J. geophys. Res.*, **78**, 3321–3333.

Snyder, D. & Bruneton, M., 2007. Seismic anisotropy of the Slave craton, NW Canada, from joint interpretation of SKS and Rayleigh waves, *Geophys. J. Int.*, **169**, 170–188.

Stankiewicz, J., Chevrot, S., van der Hilst, R.D. & de Wit, M.J., 2002. Crustal thickness, discontinuity depth, and upper mantle structure beneath southern Africa: constraints from body wave conversions, *Phys. Earth planet. Inter.*, **130**, 235–251.

Trampert, J. & Woodhouse, J.H., 2003. Global anisotropic phase velocity maps for fundamental mode surface waves between 40 and 150 s, *Geophys. J. Int.*, **154**, 154–165.

Vinnik, L.P., Green, R.W.E. & Nicolaysen, L.O., 1995. Recent deformations of the deep continental root beneath southern Africa, *Nature*, **375**, 50–52.

Vinnik, L., Kiselev, S., Weber, M., Oreshin, S. & Makeyeva L., 2012. Frozen and active seismic anisotropy beneath southern Africa, *Geophys. Res. Lett.*, **39**, L08301, doi:10.1029/2012GL051326.

Wang, Y., Wen, Y. & Weidner, D., 2008. Upper mantle SH- and P-velocity structures and compositional models beneath southern Africa, *Earth planet. Sci. Lett.*, **267**, 596–608.

Wessel, P. & Smith, W.H.F., 1995. New version of the Generic Mapping Tools released, *EOS, Trans. Am. geophys. Un.*, **76**, 329, doi:10.1029/95EO00198.

Yang, Y. & Forsyth, D.W., 2006. Regional tomographic inversion of amplitude and phase of Rayleigh waves with 2-D sensitivity kernels, *Geophys. J. Int.*, **166**, 1148–1160.

Yang, Y., Li, A. & Ritzwoller, M.H., 2008. Crustal and uppermost mantle structure in southern Africa revealed from ambient noise and teleseismic tomography, *Geophys. J. Int.*, **174**, 235–248.

Yuan, H. & Romanowicz, B., 2010. Lithospheric layering in the North American Craton, *Nature*, **466**, 1063–1068.

Zhang, X., Paulssen, H., Lebedev, S. & Meier, T., 2007. Surface wave tomography of the Gulf of California, *Geophys. Res. Lett.*, **34**, L15305, doi:10.1029/2007GL030631.

## APPENDIX A: WIDTH OF THE SLIDING WINDOWS

In this study we smoothed the measurements as a function of azimuth using sliding windows. This reduces the level of noise, by averaging the data at neighbouring azimuths. A window too wide, however, will reduce the amplitude and may bias the phase of the solutions. With a window too narrow, on the other hand, the amount of averaging may not be sufficient to reduce the level of noise.

We used a window half-width of  $15^\circ$  in all inversions mentioned above, but here we test other window widths as well. Fig. A1 (top

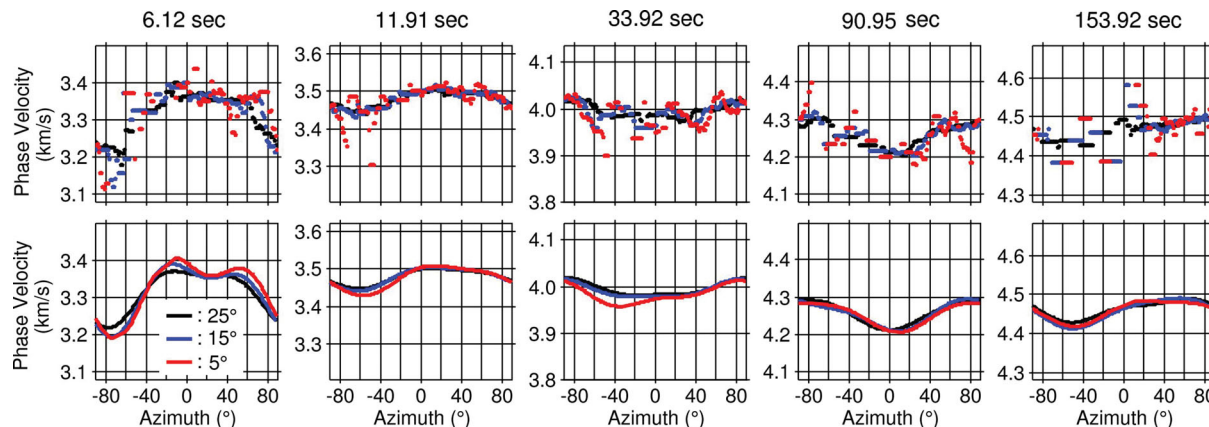


**Figure A1.** Data (top panels) and models with  $2\varphi$  and  $4\varphi$  anisotropy (bottom panels) for the Limpopo Belt region, at five different periods. Inversions of the data averaged with sliding windows of different widths produce robust results, with weak sensitivity to the window width.

panels) shows the data from the Limpopo Belt region at five periods, smoothed using three different window widths, and Fig. A1 (bottom panels) shows the results of inversions of the data, including both  $2\varphi$  and  $4\varphi$  anisotropy terms. The results show that the fast-propagation directions are weakly sensitive to the choice of the width of the sliding window and confirm that  $15^\circ$  window half-width is a reasonable choice.

## APPENDIX B: ADDITIONAL $F$ -TESTS

To complete the statistical analysis of anisotropy, we present additional tests in Fig. B1. In contrast to Fig. 6(A)/(B), where the  $2\varphi/4\varphi$

anisotropy patterns are obtained from inversions for the isotropic and both  $2\varphi$  and  $4\varphi$  terms, Fig. B1(A)/(B) shows  $2\varphi/4\varphi$  anisotropy given by inversions for only the isotropic and  $2\varphi/4\varphi$  terms. The two  $F$ -tests in Fig. B1 (C and D) are complementary to the  $F$ -tests in Fig. 6. They test the misfit improvement due to the addition of the  $4\varphi$  terms to an isotropic +  $2\varphi$  [Fig. B1(C)] and isotropic-only [Fig. B1(D)] inversion.

Comparing Fig. 6(A) ( $2\varphi$  amplitude of anisotropy and azimuth of fast propagation resulting from an inversion for  $2\varphi$  and  $4\varphi$  anisotropy) and Fig. B1(A) ( $2\varphi$  anisotropy parameters resulting from an inversion for  $2\varphi$  anisotropy only), we find the  $2\varphi$  anisotropy parameters to be nearly identical, both in their amplitude and

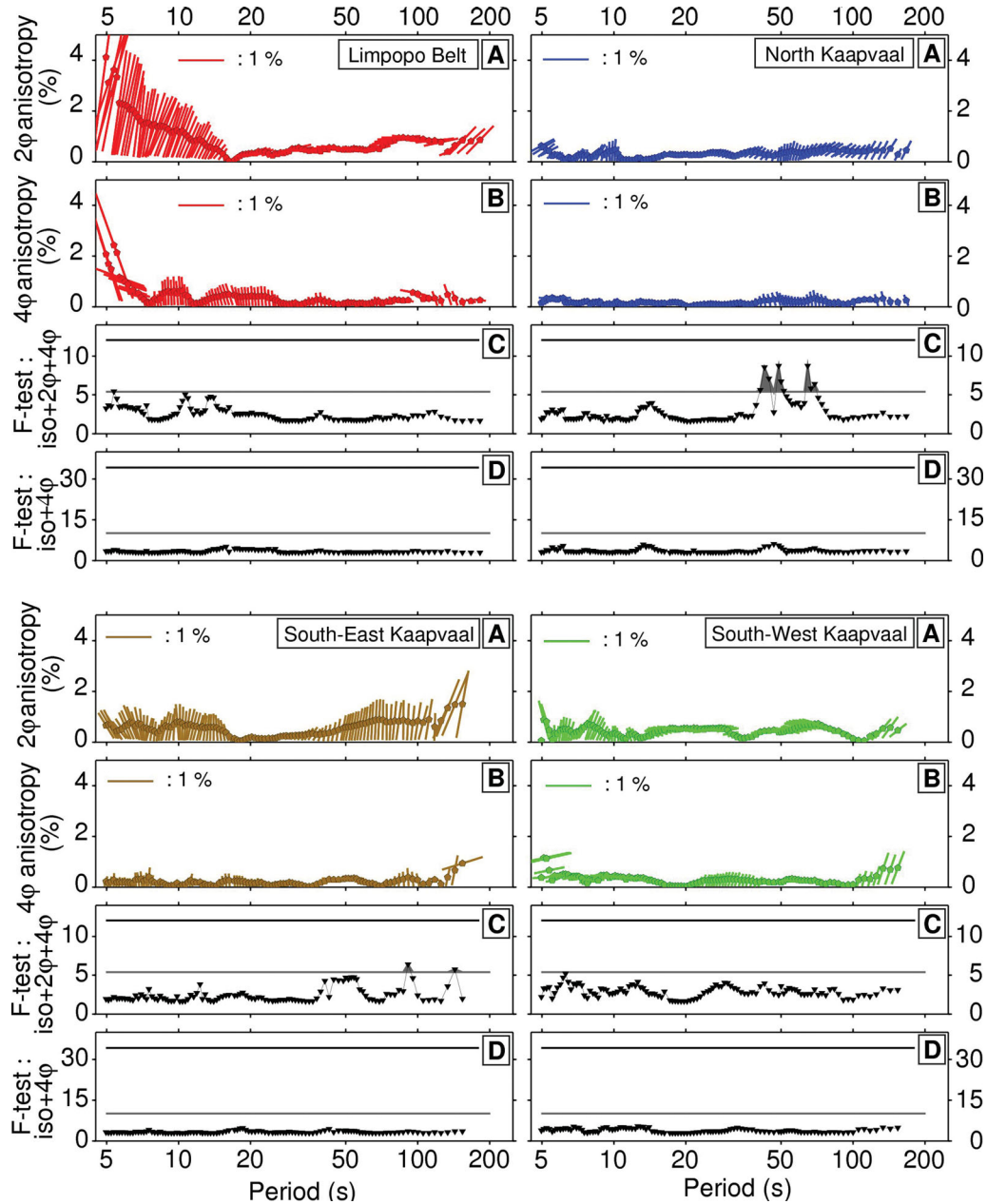


**Figure B1.** Additional results of the inversions and  $F$ -tests for the four subregions. (A) Azimuths of fast-propagation direction and amplitudes of anisotropy, from inversions for  $2\varphi$  anisotropy only. (B) Azimuths of fast direction and amplitudes of anisotropy, from inversions for  $4\varphi$  anisotropy only (for clarity, only one of the two perpendicular fast directions is shown). (C)  $F$ -tests on whether an inversion for both  $2\varphi$  and  $4\varphi$  terms improves the fit, compared to an inversion using only isotropic and  $2\varphi$  terms. (D)  $F$ -tests on whether the addition of the  $4\varphi$  terms alone improves the fit, compared to an isotropic inversion. Shaded areas indicate significance, according to the  $F$ -test. Grey: above a confidence index of 0.05.

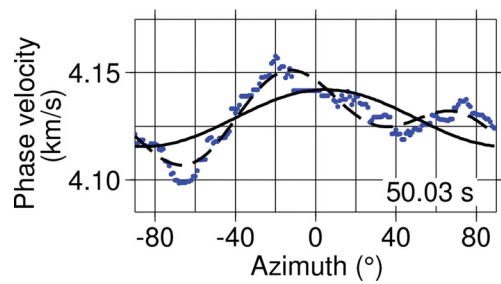


**Figure B2.** Azimuthal anisotropy at a 50.03 s period in the North Kaapvaal Craton region. Blue dots are the data, binned and smoothed with a 30° sliding window. The solid black line is the best-fitting model from an inversion with isotropic and  $2\varphi$  anisotropy parameters only. The dashed black line is the best-fitting model from an inversion with isotropic and both  $2\varphi$  and  $4\varphi$  anisotropy parameters.

direction of fast propagation. The  $2\varphi$  anisotropy in southern Africa, which we interpret and draw conclusions from, is thus robust with respect to whether or not the  $4\varphi$  parameters are included into the inversion.

Fig. B1(C) presents the  $F$ -test results on whether adding  $4\varphi$  anisotropy to an isotropic and  $2\varphi$  anisotropic inversion improves the fit. Except in the North Kaapvaal region between 33 and 83 s, adding  $4\varphi$  anisotropy does not improve the fit significantly.

In the North Kaapvaal Craton (33–83 s periods), the  $F$ -test values are greater than the threshold value with a confidence index of 0.05. Fig. B2 presents the distribution of phase velocities at a 50.03 s period in the North Kaapvaal Craton region and the best-fitting models given by the inversions with  $2\varphi$  anisotropy only and with both  $2\varphi$  and  $4\varphi$  anisotropy. At this period, the  $F$ -test shows that the data require both  $2\varphi$  and  $4\varphi$  anisotropy, and the 90° and 180° periodic patterns are clearly seen in the data.